



UNIVERSITY OF LEEDS

This is a repository copy of *Two-scale homogenization of hydrodynamic lubrication in a mechanical seal with isotropic roughness based on the Elrod cavitation algorithm*.

White Rose Research Online URL for this paper:

<https://eprints.whiterose.ac.uk/173343/>

Version: Accepted Version

Article:

Han, Y, Meng, Q orcid.org/0000-0002-6708-5585 and de Boer, G orcid.org/0000-0002-5647-1771 (2022) Two-scale homogenization of hydrodynamic lubrication in a mechanical seal with isotropic roughness based on the Elrod cavitation algorithm. Proceedings of the Institution of Mechanical Engineers, Part J: Journal of Engineering Tribology, 236 (3). pp. 359-385. ISSN 1350-6501

<https://doi.org/10.1177/13506501211017673>

This conference paper is protected by copyright. This is an author produced version of a conference paper accepted for publication in Proceedings of the Institution of Mechanical Engineers Part J: Journal of Engineering Tribology. Uploaded in accordance with the publisher's self-archiving policy.

Reuse

Items deposited in White Rose Research Online are protected by copyright, with all rights reserved unless indicated otherwise. They may be downloaded and/or printed for private study, or other acts as permitted by national copyright laws. The publisher or other rights holders may allow further reproduction and re-use of the full text version. This is indicated by the licence information on the White Rose Research Online record for the item.

Takedown

If you consider content in White Rose Research Online to be in breach of UK law, please notify us by emailing eprints@whiterose.ac.uk including the URL of the record and the reason for the withdrawal request.



eprints@whiterose.ac.uk
<https://eprints.whiterose.ac.uk/>

Two-scale homogenization of hydrodynamic lubrication in a mechanical seal with isotropic roughness based on the Elrod cavitation algorithm

Yanxiang Han^{1,2}, Qingen Meng², Gregory de Boer²

¹ School of Mechanical Engineering, Jiangsu University, Jiangsu, China

² School of Mechanical Engineering, University of Leeds, Leeds, UK

Abstract

A two-scale homogenization method for modelling the hydrodynamic lubrication of mechanical seals with isotropic roughness was developed and presents the influence of surface topography coupled into the lubricating domain. A linearization approach was derived to link the effects of surface topography across disparate scales. Solutions were calculated in a Polar coordinate system derived based on the Elrod cavitation algorithm and were determined using homogenization of periodic simulations describing the lubrication of a series of surface topographical features. Solutions obtained for the hydrodynamic lubrication regime showed that the two-scale homogenization approach agreed well with lubrication theory in the case without topography. Varying topography amplitude demonstrated that the presence of surface topography improved tribological performance for a mechanical seal in terms of increasing load-carrying capacity and reducing friction coefficient at the radial direction. A Stribeck curve analysis was conducted which indicated that including surface topography led to an increase in load carrying capacity and a reduction in friction. A study of macro-scale surface waviness showed that the micro-scale variations observed were smaller in magnitude but cannot be obtained without the two-scale method and cause significant changes in the tribological performance.

Keywords: Seals, Hydrodynamic Lubrication, Cavitation, Surface Topography, Numerical Simulation.

1 Introduction

Mechanical face seals are critical components used for rotating shafts to prevent pressurized fluid from escaping from the housing. They typically consist of a rotor and stator separated using a thin fluid film to avoid abrasive wear and attain reliable performance. The separation between the rotor and stator is achieved by fluid pressure under hydrodynamic lubrication (HL) conditions, which is generated by the rotation of the face and the fluid sealed between the rotor and stator. Seal faces typically have surface waviness ¹ due to temperature gradients, drive elements, and exposure to fluid pressures. The existence of the surface waviness causes divergent regions for the fluid where cavitation may occur. Under the assumption of an incompressible fluid, hydrodynamic cavitation leads to film rupture and a mixture of vapor and liquid phases. Considering cavitation in the lubrication analyses of mechanical face seals is very important because it can determine the accuracy of fluid pressure prediction.

Taking mass conservation into account, one significant contribution to capture rupture and reformation boundaries was presented by Jakobsson and Floberg ² and Olsson ³. The Jakobsson-Floberg-Olsson (JFO) model included both a cavitation region and full film region, this was subsequently implemented by Elrod and Adams ⁴ and developed into the well-established Elrod cavitation algorithm. This algorithm has been adopted to investigate the lubrication performance of mechanical seals ^{5, 6} considering cavitation at the macro-scale. However, these studies assumed that surfaces of the rotor and stator were perfectly smooth ⁷.

The recent study of surface topography has drawn more and more attention as it can be of a similar

scale to film thickness and therefore has a role in determining the system performance. For instance, Minet et.al⁸ pointed out that surface roughness could affect the hydrodynamic force of mechanical seal. Etsion et.al⁹ demonstrated that with proper selection of texture size and ratio in mechanical face seals, artificial surface textures could lead to higher clearance and smaller friction torque. Moreover, the cavitation at the micro-scale is equally important in lubricated mechanical seals. Hamilton et.al¹⁰ indicated that introducing micro-irregularities to parallel surfaces could result in local cavitation, which in return could greatly improve the lubrication performance between the surfaces. However, numerical modelling of surface topography and lubricated contacts simultaneously by deterministic modelling is a challenging computational problem as it requires a very fine computational mesh due to the separation of scales between surface topography and the lubricating region¹¹. Therefore, a significant amount of recent research has been presented to deal with coupling interactions between disparate scales.

The modified Reynolds equation is an effective tool to assess the lubrication behavior of two-scale features in lubricated contacts. Pioneering work presented by Patir and Cheng^{12, 13} developed an average flow model describing lubrication using flow factors to incorporate the effects of surface roughness. Based on simulations of surface features with identical statistical properties, flow factors were calculated to capture the influence of the surface roughness in the lubricant flow. This model has been widely adopted and has proved to be effective to predict the lubrication performance for a wide range of tribological applications including journal bearings¹⁴, cavitation¹⁵, and mechanical face seals¹⁶. Recently, this model was extended by Qiu and Khonsari¹⁶ to examine the role of surface roughness in the load carrying capacity improvement caused by the inclusion of surface textures.

Following Patir and Cheng's method, numerous authors employed the averaged Reynolds equations and flow factors were evaluated by various techniques¹⁷⁻¹⁹. A significant contribution to these averaged approaches was achieved by Almqvist¹⁸ who derived mathematical equations to calculate the flow factors in a local domain with the dimension of the roughness wavelength. Subsequently, the homogenized Reynolds equations inclusive of surface topography were extensively adopted for hydrodynamic lubrication. Sahlin et.al²⁰ proposed a full film lubrication model using the homogenization technique where the flow factors can be calculated for any deterministic roughness under a incompressible Newtonian flow conditions. Taking into account cavitation phenomenon, Bayada et.al²¹ incorporated the Elrod cavitation algorithm describing JFO boundary conditions to the homogenization approach by considering micro-scale cavitation due to surface roughness and macro-scale cavitation due to the diverging nature of the lubricating geometry. This research showed that the proposed method was valid for transverse and longitudinal surface roughness. All of these techniques are defined as homogenization approaches in which periodicity is imposed on the micro-scale domain and it is assumed that the homogenization procedure could produce representative results for the mechanics at both scales. Homogenization methods are applied to problems with disparate scales, which leads to an average, smooth problem in which the effects of surface roughness are included¹⁸.

Another set of homogenization methods used are based on the Heterogeneous Multiscale Methods (HMM) as proposed by Gao and Hewson²² to analyze the effect of surface texture in lubricating problems. The approach successfully solved the macro-scale pressure and film thickness for a textured surface by solving the Navier-Stokes equations together with local elastic deformations at the micro-scale and coupling micro-scale solutions to the macro-scale model by interpolating the data of the pressure gradient and mass flow rate relationship calculated at the micro-scale. Considering more practical conditions including lubricant piezoviscosity, non-Newtonian (shear-thinning) behavior and

inertial flow de Boer et.al ²³ extended the two-scale method using a metamodel describing the data from the micro- scale for tilted-pad bearings. Subsequently, based on the HMM and metamodeling de Boer et.al ²⁴ successfully minimized friction in the contacting region by optimizing surface topography, and investigated the line contacts problem ²⁵ where nonlinearities introduced by piezoviscosity, compressibility, and contact mechanics were taken into account. More recently, hydrodynamic cavitation occurring at the scale of topography was incorporated into the HMM ²⁶.

However, the above studies were all under the Cartesian coordinate system. It is intuitively easy to investigate the lubrication performance of mechanical seals under a Polar coordinate system. Therefore, it is necessary to extend the formulation of multiscale lubrication analyses to the Polar coordinate system. Therefore, in the present study, a two-scale hydrodynamic lubrication model capable of including the influence of surface topography at the micro-scale is proposed based on a finite-difference derivative-coupling procedure where the partial derivatives function in terms of lubricant flow associated with the micro-scale solutions is determined using presented linearization method. The aim of the work is to present a two-scale homogenization method in the polar coordinate system along with evaluating the influence of surface topography on the tribological performance for mechanical seals under hydrodynamic lubrication. The governing equations describing the fluid flow at both scales are derived in a Polar coordinate system. A new approach for coupling the effects of micro-scale surface topography into the macro-scale lubricating contact is introduced by utilizing mass flux derivatives and developing a coupling procedure based on finite differencing. The difficulty of this approach lies in decoupling the two scales of surface topography and the lubricated region. Assuming periodicity of surface topography, the Reynolds equation including cavitation phenomenon is derived at the micro-scale where the solutions obtained are employed to calculate the derivatives of macro-scale mass fluxes. Numerical simulations of this two-scale approach are presented for a range of topography amplitudes and the Elrod cavitation algorithm is implemented to formulate the problem with these effects included. This study is limited to an example of a mechanical seal, but can also be applicable to other engineering applications so long as HMM assumptions are maintained.

2 Theory

2.1 Macro-scale lubrication

To solve the hydrodynamic lubrication and cavitation in a mechanical face seal, the macro-scale model adopts a homogenization technique, namely the HMM, which can be employed where there is a distinct separation in scales. The macro-scale geometry of the mechanical face seal is illustrated in Figure 1 and Figure 2, showing a section of the seal faces with axial-symmetry. The inner radius is R_1 and the outer radius is R_0 , the face angle of the periodic section is Ψ_0 . It is assumed that the upper face rotates with an angular speed ω about the axis and the lower face is stationary. The gap between the two faces is filled with an isoviscous, incompressible, and Newtonian lubricant, and it is assumed that the two seal faces are fully separated by fluid film. Additionally, the rotating face is modelled as perfectly smooth and flat and the lower face includes surface topography. The film thickness functions representing surface topography for both surfaces can be reduced to a single film thickness function by superimposing the roughness to one surface. This simplification can still model the problem accurately under steady-state conditions and does not influence the efficiency of the method presented. The dynamic case in which there is relative motion both of rough surfaces within the model framework is yet to be established. Both faces are made of steel, therefore the surface deformation caused by the pressures observed at macro- and micro-scale is negligible (see Section 3.1). For the macro-scale

model, lubricant flow between the seal faces is described by the Reynolds equations and JFO conditions under isothermal operating conditions. Note that the two bounding surfaces are parallel in Figure 1, but they are in fact with surface profile as shown in Figure 2. A nomenclature is given in Appendix A in accordance with the terms used throughout this manuscript.

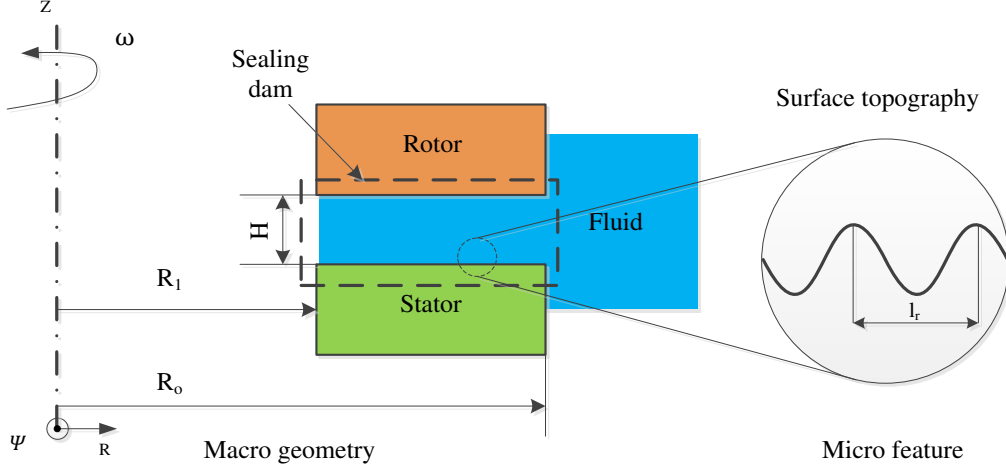


Figure 1 Diagram of Mechanical Face Seal

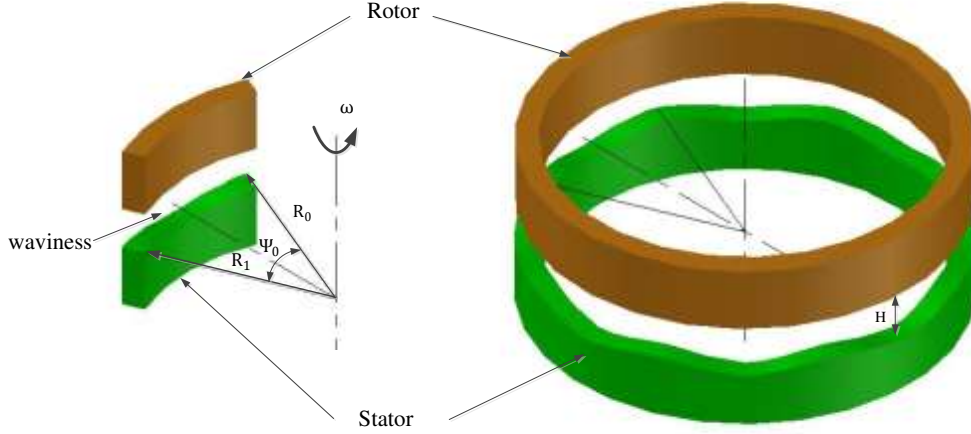


Figure 2 Macro-scale geometry

2.1.1 Macro-scale variables and geometry

To ensure that the results produced are scalable across parameter regimes all variables have been made non-dimensional in this work. The non-dimensional variables at the macro-scale are given in (1), and a full description of the non-dimensional form of the macro-scale model is derived in the following sub-sections.

$$\bar{R} = \frac{R}{R_0} \quad \bar{H}, \bar{H}_0, \bar{A} = \frac{H, H_0, A}{H_{00}} \quad \bar{\Psi} = \Psi \quad \bar{G} = \frac{G}{\lambda} \quad \bar{\Theta} = \frac{\Theta}{\lambda} \quad \bar{Q}_{\bar{R}, \bar{\Psi}} \quad (1)$$

$$= \frac{2Q_{R, \Psi}}{\rho_0 \omega H_{00} R_0}$$

$$\bar{P}, \bar{P}_0, \bar{P}_1, \bar{P}_c = \frac{P, P_0, P_1, P_c}{\lambda^2 \beta} \quad \lambda = \frac{6\eta\omega R_0^2}{\beta H_{00}^2}$$

Note that H_{00} is a scaling film thickness used only for non-dimensionalisation, which is different from

the minimum film thickness H_0 . G denotes switch function which is determined by the density ratio Θ . The fluid pressure P is subsequently defined by the Elrod model, see Section 2.1.2.

The film thickness between two lubricated seal faces contains a given film separation, and the ideal surface waviness. The circumferential variation of film thickness is a common assumption for mechanical seals as addressed in the previous literature¹⁻⁷. In this work the non-dimensional equation of the film thickness is represented as equation (2),

$$\bar{H} = \bar{H}_0 + \frac{\bar{A}}{2} \cos(n_w \bar{\Psi}) \quad (2)$$

where \bar{H}_0 is the non-dimensional minimum film thickness, \bar{A} denotes the non-dimensional amplitude of the waviness at the macro-scale as shown in Figure 2, and n_w represents the number of surface waves on the circumference of a face seal. Note that while there is no radial variation in macro-scale film thickness that this is not beyond the capacity of the method or solution procedure described in this article.

2.1.2 Macro-scale Elrod model

To facilitate the analysis, modelling of the mechanical face seal is naturally carried out using the Polar coordinates. Two-dimensional fluid flow model including the cavitation phenomenon due to the convergent-divergent shape is considered at the macro-scale. More complex fluid properties exist such as pressure-dependent rheology, compressibility, and non-Newtonian viscosity. However, the pressure is low as described and so piezo-viscosity and compressibility have little effect here but can be included in the present model. Non-Newtonian flow can also be considered but here a fair first step assumption for the lubricant in seals is that it is Newtonian and the shear rate is relatively constant throughout the seal. These effects have been explored using the HMM in lubrication by de Boer, et al.²³ and the two-scale method can be readily adapted to include these phenomena where necessary. By substituting the non-dimensional variables defined in section 2.1.2 into the macro-scale model, governing equations are derived from mass continuity under steady-state conditions (equation (3)),

$$\frac{1}{\bar{R}} \frac{\partial(\bar{R}\bar{Q}_R)}{\partial\bar{R}} + \frac{1}{\bar{R}} \frac{\partial\bar{Q}_\Psi}{\partial\bar{\Psi}} = 0 \quad (3)$$

and in combination with the definition of the switch function \bar{G} and fluid pressure \bar{P} from equations (4) and (5) respectively,

$$\bar{G} = \begin{cases} \frac{1}{\lambda} & \bar{\Theta} > \frac{1}{\lambda} \\ 0 & \bar{\Theta} \leq \frac{1}{\lambda} \end{cases} \quad (4)$$

$$\bar{P} = \bar{P}_c + \bar{G}(\bar{\Theta} - \frac{1}{\lambda}) \quad (5)$$

the mass fluxes \bar{Q}_R and \bar{Q}_Ψ become (6) and (7),

$$\bar{Q}_R = -\lambda\bar{G}\bar{H}^3 \frac{\partial\bar{\Theta}}{\partial\bar{R}} \quad (6)$$

$$\bar{Q}_\Psi = \lambda \left(-\bar{G} \frac{\bar{H}^3}{\bar{R}} \frac{\partial\bar{\Theta}}{\partial\bar{\Psi}} + \bar{\Theta}\bar{H}\bar{R} \right) \quad (7)$$

Substituting these two equations into equation (3) results in the Elrod model for fluid flow at the macro-scale (equation (8)),

$$\frac{\partial}{\partial \bar{R}} \left[\bar{G} \bar{R} \bar{H}^3 \frac{\partial \bar{\Theta}}{\partial \bar{R}} \right] + \frac{1}{\bar{R}} \frac{\partial}{\partial \bar{\Psi}} \left[\bar{G} \bar{H}^3 \frac{\partial \bar{\Theta}}{\partial \bar{\Psi}} \right] = \bar{R} \frac{\partial(\bar{\Theta} \bar{H})}{\partial \bar{\Psi}} \quad (8)$$

in the domain $\Omega_{\text{macro}} = \left\{ \frac{R_1}{R_0} \leq \bar{R} \leq 1, 0 \leq \bar{\Psi} \leq \Psi_0 \right\}$.

In the non-dimensional form, the two variants of equation (8) become equations (9) and (10),

$$\frac{\partial}{\partial \bar{R}} \left[\bar{R} \bar{H}^3 \frac{\partial \bar{\Theta}}{\partial \bar{R}} \right] + \frac{1}{\bar{R}} \frac{\partial}{\partial \bar{\Psi}} \left[\bar{H}^3 \frac{\partial \bar{\Theta}}{\partial \bar{\Psi}} \right] = \lambda \bar{R} \frac{\partial(\bar{\Theta} \bar{H})}{\partial \bar{\Psi}}, \bar{G} = \frac{1}{\lambda} \quad (9)$$

$$\frac{\partial(\bar{\Theta} \bar{H})}{\partial \bar{\Psi}} = 0, \bar{G} = 0 \quad (10)$$

which correspond to the liquid and cavitation regions respectively.

2.1.3 General form of the macro-scale model

Assuming the existence of surface topography, the traditional Reynolds equation and Elrod model are not applicable. Therefore a general form of two-dimensional fluid flow is instead presented using equations (11) and (12) to describe mass fluxes in the case of cavitation phenomenon,

$$\bar{Q}_{\bar{R}} = f \left(\bar{\Theta}, \frac{\partial \bar{\Theta}}{\partial \bar{R}}, \frac{\partial \bar{\Theta}}{\partial \bar{\Psi}}, \bar{H}, \bar{R}, \bar{\Psi} \right) \quad (11)$$

$$\bar{Q}_{\bar{\Psi}} = f \left(\bar{\Theta}, \frac{\partial \bar{\Theta}}{\partial \bar{R}}, \frac{\partial \bar{\Theta}}{\partial \bar{\Psi}}, \bar{H}, \bar{R}, \bar{\Psi} \right) \quad (12)$$

here, $\bar{Q}_{\bar{R}}$ and $\bar{Q}_{\bar{\Psi}}$ are non-dimensional macro-scale mass fluxes in the radial and angular directions, respectively, which are functions of the six variables $\bar{\Theta}, \frac{\partial \bar{\Theta}}{\partial \bar{R}}, \frac{\partial \bar{\Theta}}{\partial \bar{\Psi}}, \bar{H}, \bar{R}, \bar{\Psi}$. The dependency is a result of the coupling between the macro- and micro-scale models in which homogenized relationship for mass flux across these parameters is introduced.

Substituting equations (11) and (12) into equation (3) for mass continuity, the partial derivative format of the governing equation is expressed in terms of the four independent variables $\bar{\Theta}, \frac{\partial \bar{\Theta}}{\partial \bar{R}}, \frac{\partial \bar{\Theta}}{\partial \bar{\Psi}}, \bar{H}$, where $\bar{\Theta}, \frac{\partial \bar{\Theta}}{\partial \bar{R}}, \frac{\partial \bar{\Theta}}{\partial \bar{\Psi}}, \bar{H} = f(\bar{R}, \bar{\Psi})$. This yields equation (13),

$$\begin{aligned} & \frac{\partial(\bar{R} \bar{Q}_{\bar{R}})}{\partial \bar{\Theta}} \frac{\partial \bar{\Theta}}{\partial \bar{R}} + \frac{\partial(\bar{R} \bar{Q}_{\bar{R}})}{\partial \left(\frac{\partial \bar{\Theta}}{\partial \bar{R}} \right)} \frac{\partial}{\partial \bar{R}} \left(\frac{\partial \bar{\Theta}}{\partial \bar{R}} \right) + \frac{\partial(\bar{R} \bar{Q}_{\bar{R}})}{\partial \left(\frac{\partial \bar{\Theta}}{\partial \bar{\Psi}} \right)} \frac{\partial}{\partial \bar{R}} \left(\frac{\partial \bar{\Theta}}{\partial \bar{\Psi}} \right) + \frac{\partial(\bar{R} \bar{Q}_{\bar{R}})}{\partial \bar{H}} \frac{\partial \bar{H}}{\partial \bar{R}} + \frac{\partial \bar{Q}_{\bar{\Psi}}}{\partial \bar{\Theta}} \frac{\partial \bar{\Theta}}{\partial \bar{\Psi}} \\ & + \frac{\partial \bar{Q}_{\bar{\Psi}}}{\partial \left(\frac{\partial \bar{\Theta}}{\partial \bar{R}} \right)} \frac{\partial}{\partial \bar{\Psi}} \left(\frac{\partial \bar{\Theta}}{\partial \bar{R}} \right) + \frac{\partial \bar{Q}_{\bar{\Psi}}}{\partial \left(\frac{\partial \bar{\Theta}}{\partial \bar{\Psi}} \right)} \frac{\partial}{\partial \bar{\Psi}} \left(\frac{\partial \bar{\Theta}}{\partial \bar{\Psi}} \right) + \frac{\partial \bar{Q}_{\bar{\Psi}}}{\partial \bar{H}} \frac{\partial \bar{H}}{\partial \bar{\Psi}} = 0 \end{aligned} \quad (13)$$

in which the partial derivatives are informed by results generated at the micro-scale. A special case of equation (13) is that the size of the micro-scale domain is zero and surface topography could be neglected. The Reynolds equation of such a case is obtained from equation (3) and presented in Appendix B.

2.1.4 Macro-scale boundary conditions

The boundary conditions governing the behavior of fluid flow of the non-dimensional macro-scale model are prescribed by given pressures at the global inlet and outlet of the seal, i.e. equations (14) and (15),

$$\bar{P}(1, \bar{\Psi}) = \bar{P}_0, \quad \bar{P}_0 \geq 0 \quad (14)$$

$$\bar{P}\left(\frac{R_1}{R_0}, \bar{\Psi}\right) = \bar{P}_1, \quad \bar{P}_1 \geq 0 \quad (15)$$

since the density ratio is the primary variable of the macro-scale problem when cavitation effect is introduced, the boundary conditions at the inlet and outlet are expressed as Dirichlet conditions in equations (16) and (17).

$$\bar{\Theta}(1, \bar{\Psi}) = \bar{P}_0 - \bar{P}_c + \frac{1}{\lambda} \quad (16)$$

$$\bar{\Theta}\left(\frac{R_1}{R_0}, \bar{\Psi}\right) = \bar{P}_1 - \bar{P}_c + \frac{1}{\lambda} \quad (17)$$

In the angular direction, periodic boundary conditions are adopted due to the periodic physical geometry of the mechanical seal (18),

$$\bar{\Theta}(\bar{R}, 0) = \bar{\Theta}(\bar{R}, \Psi_0) \quad (18)$$

mass conservation in the angular direction can then be applied to keep the balance of mass flux at the macro-scale boundaries (19),

$$(n_{\bar{R}} \bar{Q}_{\bar{R}} + n_{\bar{\Psi}} \bar{Q}_{\bar{\Psi}})_{\bar{R},0} = -(n_{\bar{R}} \bar{Q}_{\bar{R}} + n_{\bar{\Psi}} \bar{Q}_{\bar{\Psi}})_{\bar{R},\Psi_0} \quad (19)$$

which becomes (20),

$$n_{\bar{R},0} (\bar{Q}_{\bar{R},0} - \bar{Q}_{\bar{R},\Psi_0}) + n_{\bar{\Psi},0} (\bar{Q}_{\bar{\Psi},0} - \bar{Q}_{\bar{\Psi},\Psi_0}) = 0 \quad (20)$$

in which the normal coordinate directions of the boundary are given by (21) and (22),

$$n_{\bar{R},0} = 0 \quad (21)$$

$$n_{\bar{\Psi},0} = -1 \quad (22)$$

and results in (23).

$$\bar{Q}_{\bar{\Psi},\Psi_0} - \bar{Q}_{\bar{\Psi},0} = 0 \quad (23)$$

Substituting equation (7) into equation (23) yields (24),

$$\left(-\bar{G} \frac{\bar{H}^3}{\bar{R}} \frac{\partial \bar{\Theta}}{\partial \bar{\Psi}} + \bar{\Theta} \bar{H} \bar{R}\right)_{\bar{R},\Psi_0} - \left(-\bar{G} \frac{\bar{H}^3}{\bar{R}} \frac{\partial \bar{\Theta}}{\partial \bar{\Psi}} + \bar{\Theta} \bar{H} \bar{R}\right)_{\bar{R},0} = 0 \quad (24)$$

under the assumption of periodic physical geometry in the circumferential direction of a mechanical seal, the film thickness at opposite sides are equal in one period of the seal surface, leading to the following equations (25), (26), (27) and (28),

$$\bar{R}(\bar{R}, \Psi_0) = \bar{R}(\bar{R}, 0) \quad (25)$$

$$\bar{H}(\bar{R}, \Psi_0) = \bar{H}(\bar{R}, 0) \quad (26)$$

$$\bar{G}(\bar{R}, \Psi_0) = \bar{G}(\bar{R}, 0) \quad (27)$$

$$\bar{\Theta}(\bar{R}, \Psi_0) = \bar{\Theta}(\bar{R}, 0) \quad (28)$$

following from this and rearranging leads to (29),

$$\left(\bar{G} \frac{\bar{H}^3}{\bar{R}} \frac{\partial \bar{\Theta}}{\partial \bar{\Psi}}\right)_{\bar{R},\Psi_0} - \left(\bar{G} \frac{\bar{H}^3}{\bar{R}} \frac{\partial \bar{\Theta}}{\partial \bar{\Psi}}\right)_{\bar{R},0} = (\bar{\Theta} \bar{H} \bar{R})_{\bar{R},\Psi_0} - (\bar{\Theta} \bar{H} \bar{R})_{\bar{R},0} \quad (29)$$

which is reduced to (30),

$$\left(\frac{\partial \bar{\Theta}}{\partial \bar{\Psi}}\right)_{\bar{R},\Psi_0} - \left(\frac{\partial \bar{\Theta}}{\partial \bar{\Psi}}\right)_{\bar{R},0} = 0 \quad (30)$$

to give the final form of the Neumann boundary condition for the density ratio.

2.1.5 Load capacity

Solving equations for the density ratio subject to specified boundary conditions produces the solution

to the macro-scale problem. The fluid pressure is calculated from the density ratio using equation (5). The load-carrying capacity for the mechanical seal is subsequently described by (31),

$$\bar{L} = \int_{\frac{R_1}{R_0}}^1 \int_0^{\Psi_0} \bar{P}^* \bar{R}(\bar{R}, \bar{\Psi}) d\bar{\Psi} d\bar{R} \quad (31)$$

here, \bar{P}^* is an average cell pressure derived from the micro-scale and quantifies the load per unit area acting at the macro-scale. The macro-scale load per unit area \bar{P}^* , and pressure \bar{P} differ as pressure is not linearly distributed in the micro-scale fluid domain due to the effects of surface topography and cavitation. At the macro-scale the load carrying capacity of the mechanical seal is determined from the load per unit \bar{P}^* calculated by equation (32),

$$\bar{P}^* = \bar{P}_c + \bar{G}^* \left(\bar{\Theta}^* - \frac{1}{\lambda} \right) \quad (32)$$

where $\bar{\Theta}^*$ is a homogenized parameter at the micro-scale, which is different from $\bar{\Theta}$ due to the effects of surface topography, , and \bar{G}^* is determined using equation (33).

$$\bar{G}^* = \begin{cases} \frac{1}{\lambda} & \bar{\Theta}^* > \frac{1}{\lambda} \\ 0 & \bar{\Theta}^* \leq \frac{1}{\lambda} \end{cases} \quad (33)$$

The non-dimensional forms of \bar{L} , \bar{P}^* and \bar{G}^* are derived from the scaling given in (34).

$$\bar{L} = \frac{L}{R_0^2 \lambda^2 \beta} \quad \bar{P}^* = \frac{P^*}{\lambda^2 \beta} \quad \bar{G} = \frac{G^*}{\lambda} \quad \bar{\Theta}^* = \frac{\Theta^*}{\lambda} \quad (34)$$

2.1.6 Friction

Fluid transport leads to shear stresses acting in the fluid due to viscosity. The friction force is defined as the integration of shear stresses acting over the computational domain. The expressions of shear stresses in the radial and angular directions are given in this section.

For the single-scale case shear stresses in the radial and angular directions are calculated from equation (35) and (36) at the macro-scale, respectively

$$\bar{T}_{\bar{R}1,2} = \pm \lambda \bar{G} \bar{H} \frac{\partial \bar{\Theta}}{\partial \bar{R}} \quad (35)$$

$$\bar{T}_{\bar{\Psi}1,2} = \pm \lambda \frac{\bar{G} \bar{H}}{\bar{R}} \frac{\partial \bar{\Theta}}{\partial \bar{\Psi}} + \frac{1}{3} \frac{\bar{R}}{\bar{H}} \quad (36)$$

where the subscripts 1 and 2 refer to the upper and lower surfaces of the macro-scale domain respectively. The friction force is then derived by integrating the shear stresses over the macro-scale domain (equation (37)).

$$\bar{F}_{\bar{R}, \bar{\Psi}1,2} = \int_{\frac{R_1}{R_0}}^1 \int_0^{\Psi_0} \bar{T}_{\bar{R}, \bar{\Psi}1,2} \bar{R}(\bar{R}, \bar{\Psi}) d\bar{\Psi} d\bar{R} \quad (37)$$

In the two-scale case $\bar{T}_{\bar{R}, \bar{\Psi}1,2}$ are average shear stresses at the micro-scale domain, which are derived from homogenized equation (68) in Section 2.2.2. The friction coefficient is expressed by the ratio of the friction force and load carrying capacity, see equation (38).

$$\mu_{R, \Psi1,2} = \frac{F_{R, \Psi1,2}}{L} = \frac{H_{00}}{2R_0 \lambda} \cdot \frac{\bar{F}_{\bar{R}, \bar{\Psi}1,2}}{\bar{L}} \quad (38)$$

A series of friction coefficients are obtained to present a Stribeck curve by varying the minimum film

thickness \bar{H}_0 and evaluating the effect of surface topography on the performance of mechanical seal. For the purpose a modified Sommerfeld number S is defined by equation (39).

$$S = \frac{(R_0 + R_1)(R_0 - R_1)}{2} \cdot \frac{\omega\eta}{L} = \left(1 + \frac{R_1}{R_0}\right) \left(1 - \frac{R_1}{R_0}\right) \frac{\omega\eta}{2\lambda^2\beta\bar{L}} \quad (39)$$

The non-dimensional forms of $\bar{T}_{\bar{R},\bar{\Psi}_{1,2}}$ and $\bar{F}_{\bar{R},\bar{\Psi}_{1,2}}$ are obtained from equation (40).

$$\bar{T}_{\bar{R},\bar{\Psi}_{1,2}} = \frac{2R_0 T_{R,\Psi_{1,2}}}{\lambda\beta H_{00}} \quad \bar{F}_{\bar{R},\bar{\Psi}_{1,2}} = \frac{2F_{R,\Psi_{1,2}}}{\lambda\beta H_{00} R_0} \quad (40)$$

2.2 Micro-scale lubrication

The micro-scale model shown in Figure 3 considers a subdomain independent of the mechanical face seal, in which a density ratio $\bar{\Theta}$, density ratio gradients $\frac{\partial\bar{\Theta}}{\partial\bar{R}}$ and $\frac{\partial\bar{\Theta}}{\partial\bar{\Psi}}$, and film thickness \bar{H} are inherited from the macro-scale model to determine the parameters of the micro-scale model. In order to satisfy the HMM, two assumptions must hold: (i) the size of the micro-scale domain must be at least an order of magnitude smaller than that of the macro-scale domain; (ii) periodicity in geometry dimensions and flow parameters is maintained at the boundaries of the micro-scale model.

The geometry of the micro-scale model is shown in Figure 3, and the micro-scale domain is specified by $\Omega_{\text{micro}} = \left\{ \bar{R} - \frac{l_{\bar{r}}}{2} \leq \bar{r} \leq \bar{R} + \frac{l_{\bar{r}}}{2}, \bar{\Psi} - \frac{l_{\bar{\psi}}}{2} \leq \bar{\psi} \leq \bar{\Psi} + \frac{l_{\bar{\psi}}}{2} \right\}$, where \bar{r} and $\bar{\psi}$ are the micro-scale Polar coordinate directions. The value of each $l_{\bar{r}}$ and $l_{\bar{\psi}}$ depends on the value of ϵ defining the separation of the scales in the problem $l_{\bar{r}}, l_{\bar{\psi}} = \epsilon(l_{\bar{R}}, l_{\bar{\Psi}})$, where $l_{\bar{R}} = 1 - \frac{R_1}{R_0}, l_{\bar{\Psi}} = \Psi_0$ define the size of the macro-scale domain in each coordinate direction. The value of the separation in scales ϵ must be selected as at least an order of magnitude or less than the size of the computational domain at the macro-scale, e.g., $\epsilon < 10^{-1}$. This separation in scales satisfies the assumption of the near-parallel contacting surfaces used in deriving the macro-scale Elrod model. Due to periodicity in the geometry and flow parameters at the micro-scale, as ϵ tends to zero then the solution to the micro-scale problem tends to the exact value as described by the Reynolds equation. Conversely, if ϵ increases beyond this limit then the assumption of near-parallel in contacting surface represented by the HMM breaks down. Surface topography is assumed isotropic in this study in which a constant geometry of the micro-scale is considered for each of the macro-scale simulations, variation in the micro-scale geometry within the macro-scale can be facilitated by HMM so long as the variation is continuously distributed and the assumptions underpinning the two-scale model are maintained.

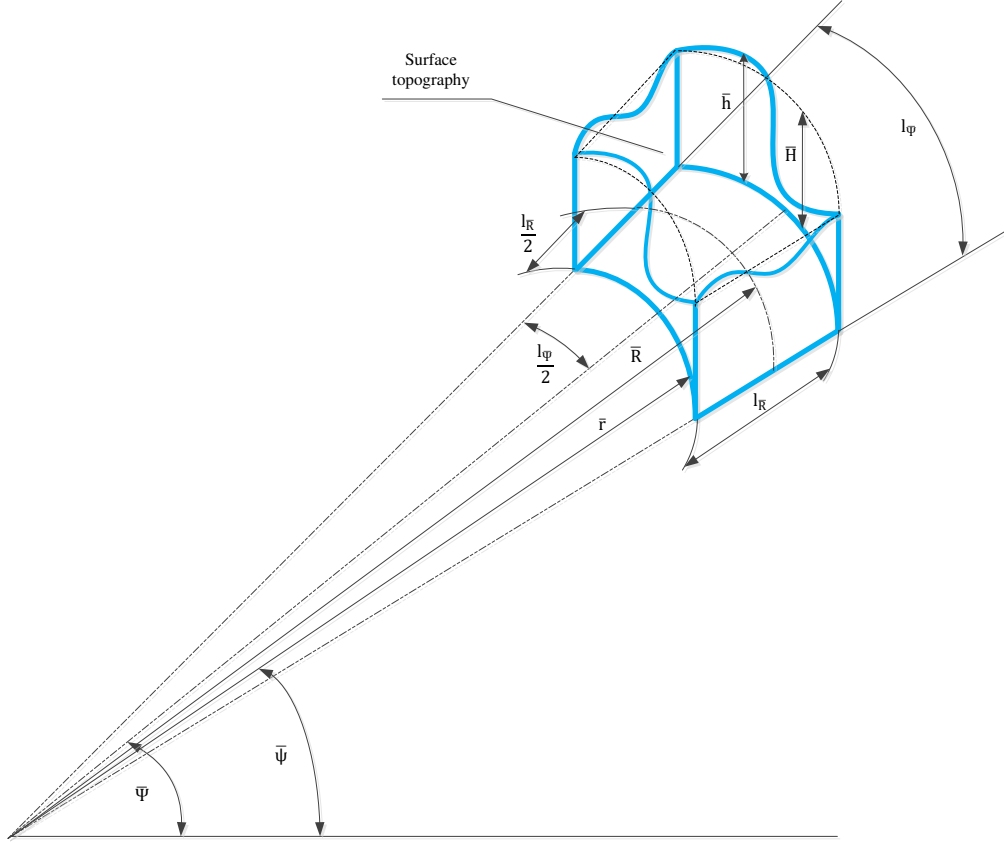


Figure 3 Micro-scale geometry

2.2.1 Micro-scale variables and geometry

At the micro-scale, fluid flow is modelled using the Reynolds equation with cavitation included by the Elrod model. For the consideration of mass conservation in the lubricant, flow is considered steady, Newtonian, incompressible, isoviscous, and isothermal as is consistent with the conditions imposed at the macro-scale. Considering the following non-dimensionalization (equation (41)),

$$\begin{aligned} \bar{r} &= \frac{r}{R_0} & \bar{h}, \bar{h}_t, \bar{A}_t &= \frac{h, h_t, A_t}{H_{00}} & \bar{\psi} &= \psi & \bar{g} &= \frac{g}{\lambda} & \bar{\theta} &= \frac{\theta}{\lambda} \\ \bar{q}_{r,\bar{\psi}} &= \frac{2q_{r,\psi}}{\rho_0 \omega H_{00} R_0} & \bar{\tau}_{r,\bar{\psi}_{1,2}} &= \frac{2R_0 \tau_{r,\psi_{1,2}}}{\lambda \beta H_{00}} & \bar{p} &= \frac{p}{\lambda^2 \beta} \end{aligned} \quad (41)$$

the governing equation for the fluid transport at the micro-scale domain Ω_{micro} is described by the non-dimensional form equation (42),

$$\frac{\partial}{\partial \bar{r}} \left[\bar{g} \bar{r} \bar{h}^3 \frac{\partial \bar{\theta}}{\partial \bar{r}} \right] + \frac{1}{\bar{r}} \frac{\partial}{\partial \bar{\psi}} \left[\bar{g} \bar{h}^3 \frac{\partial \bar{\theta}}{\partial \bar{\psi}} \right] = \bar{r} \frac{\partial (\bar{\theta} \bar{h})}{\partial \bar{\psi}} \quad (42)$$

where $\bar{\theta}$ is the non-dimensional density ratio at the micro-scale, \bar{h} is the non-dimensional film thickness, \bar{g} is defined as following (equation (43)).

$$\bar{g} = \begin{cases} \frac{1}{\lambda} & \bar{\theta} > \frac{1}{\lambda} \\ 0 & \bar{\theta} \leq \frac{1}{\lambda} \end{cases} \quad (43)$$

Once solving for the density ratio in (42) the fluid pressure is given by equation (44),

$$\bar{p} = \bar{P}_c + \bar{g} \left(\bar{\theta} - \frac{1}{\lambda} \right) \quad (44)$$

and the micro-scale mass fluxes are expressed by equations (45) and (46).

$$\bar{q}_r = -\lambda \bar{g} \bar{h}^3 \frac{\partial \bar{\theta}}{\partial \bar{r}} \quad (45)$$

$$\bar{q}_\psi = \lambda \left(-\bar{g} \frac{\bar{h}^3}{\bar{r}} \frac{\partial \bar{\theta}}{\partial \bar{\psi}} + \bar{\theta} \bar{h} \bar{r} \right) \quad (46)$$

The film thickness at the micro-scale is described by macro-scale film thickness and surface topography, which is represented by equation (47),

$$\bar{h} = \bar{H} + \bar{h}_t \quad (47)$$

where \bar{h}_t is the periodic function describing surface topography, and \bar{H} is the film thickness at the macro-scale. The function describing surface topography must be periodic in the micro-scale film thickness at the boundaries in order to satisfy the requirement of two-scale theory. Equation (48) is selected for the purpose of this study,

$$\bar{h}_t = \frac{\bar{A}_t}{2} \cos \left(\frac{2\pi \bar{r}}{\bar{l}_r} \right) \cos \left(\frac{2\pi \bar{\psi}}{\bar{l}_\psi} \right) \quad (48)$$

where \bar{A}_t is the non-dimensional micro-scale topography amplitude. A value of $\bar{A}_t = 0$ corresponds to a smooth case, where the problem can be directly described by Reynolds equation at the macro-scale. In addition, if the length scales of the micro-scale domain diminish to zero, then the topographical feature vanishes and the solution obtained at the micro-scale is the exact solution to the Reynolds equation at the macro-scale for the same conditions.

In addition, the micro-scale shear stresses $\bar{\tau}_{r,1,2}$ and $\bar{\tau}_{\psi,1,2}$ are defined as,

$$\bar{\tau}_{r,1,2} = \pm \lambda \bar{g} \bar{h} \frac{\partial \bar{\theta}}{\partial \bar{r}} \quad (49)$$

$$\bar{\tau}_{\psi,1,2} = \pm \lambda \frac{\bar{g} \bar{h}}{\bar{r}} \frac{\partial \bar{\theta}}{\partial \bar{\psi}} + \frac{1}{3} \frac{\bar{r}}{\bar{h}} \quad (50)$$

where the subscripts 1 and 2 refer to the upper and lower surfaces of the micro-scale domain respectively.

2.2.2 Micro-scale boundary conditions

The solution to equation (42) is achieved by specifying periodic boundary conditions for the density ratio at the boundaries of the micro-scale subdomain. Both periodic conditions and mass conservation should be satisfied for each set of boundaries and four corner nodes at the subdomain simultaneously. Periodic conditions are imposed such that the profiles of density ratio on each set of boundaries are equal where the magnitudes are shifted by $\Delta_{\bar{\theta},\bar{r}}$ and $\Delta_{\bar{\theta},\bar{\psi}}$ in each of the coordinate directions, respectively. Therefore, equations (51) and (52) are obtained,

$$\bar{\theta} \left(\bar{R} - \frac{l_r}{2}, \bar{\Psi} \right) = \bar{\theta} \left(\bar{R} + \frac{l_r}{2}, \bar{\Psi} \right) - \Delta_{\bar{\theta},\bar{r}} \quad (51)$$

$$\bar{\theta} \left(\bar{R}, \bar{\Psi} - \frac{l_\psi}{2} \right) = \bar{\theta} \left(\bar{R}, \bar{\Psi} + \frac{l_\psi}{2} \right) - \Delta_{\bar{\theta},\bar{\psi}} \quad (52)$$

where $\Delta_{\bar{\theta},\bar{r}}$ and $\Delta_{\bar{\theta},\bar{\psi}}$ are determined from the homogenized gradients of the density ratio at the macro-scale using equations (53) and (54).

$$\Delta_{\bar{\theta}, \bar{r}} = \frac{\partial \bar{\theta}}{\partial \bar{r}} l_{\bar{r}} \quad (53)$$

$$\Delta_{\bar{\theta}, \bar{\psi}} = \frac{\partial \bar{\theta}}{\partial \bar{\psi}} l_{\bar{\psi}} \quad (54)$$

Subsequently, imposing mass conservation conditions at the subdomain leads to equations (55) and (56) applicable for opposing sides of this subdomain except for the four corner nodes.

$$\left(\frac{\partial \bar{\theta}}{\partial \bar{r}} \right)_{\bar{R} - \frac{l_{\bar{r}}}{2}, \bar{\Psi}} - \left(\frac{\partial \bar{\theta}}{\partial \bar{r}} \right)_{\bar{R} + \frac{l_{\bar{r}}}{2}, \bar{\Psi}} = 0 \quad (55)$$

$$\left(\frac{\partial \bar{\theta}}{\partial \bar{\psi}} \right)_{\bar{R}, \bar{\Psi} - \frac{l_{\bar{\psi}}}{2}} - \left(\frac{\partial \bar{\theta}}{\partial \bar{\psi}} \right)_{\bar{R}, \bar{\Psi} + \frac{l_{\bar{\psi}}}{2}} = 0 \quad (56)$$

Periodic conditions are applied on the four corner nodes (equations (57), (58), (59) and (60)).

$$\bar{\theta} \left(\bar{R} - \frac{l_{\bar{r}}}{2}, \bar{\Psi} - \frac{l_{\bar{\psi}}}{2} \right) = \bar{\theta} \left(\bar{R} + \frac{l_{\bar{r}}}{2}, \bar{\Psi} - \frac{l_{\bar{\psi}}}{2} \right) - \Delta_{\bar{\theta}, \bar{r}} \quad (57)$$

$$\bar{\theta} \left(\bar{R} - \frac{l_{\bar{r}}}{2}, \bar{\Psi} - \frac{l_{\bar{\psi}}}{2} \right) = \bar{\theta} \left(\bar{R} - \frac{l_{\bar{r}}}{2}, \bar{\Psi} + \frac{l_{\bar{\psi}}}{2} \right) - \Delta_{\bar{\theta}, \bar{\psi}} \quad (58)$$

$$\bar{\theta} \left(\bar{R} + \frac{l_{\bar{r}}}{2}, \bar{\Psi} + \frac{l_{\bar{\psi}}}{2} \right) = \bar{\theta} \left(\bar{R} - \frac{l_{\bar{r}}}{2}, \bar{\Psi} + \frac{l_{\bar{\psi}}}{2} \right) + \Delta_{\bar{\theta}, \bar{r}} \quad (59)$$

$$\bar{\theta} \left(\bar{R} + \frac{l_{\bar{r}}}{2}, \bar{\Psi} + \frac{l_{\bar{\psi}}}{2} \right) = \bar{\theta} \left(\bar{R} + \frac{l_{\bar{r}}}{2}, \bar{\Psi} - \frac{l_{\bar{\psi}}}{2} \right) + \Delta_{\bar{\theta}, \bar{\psi}} \quad (60)$$

Similarly, four equations derived from mass conservation conditions for the four corner nodes (equations (61), (62), (63) and (64)).

$$\left(\frac{\partial \bar{\theta}}{\partial \bar{r}} \right)_{\bar{R} + \frac{l_{\bar{r}}}{2}, \bar{\Psi} - \frac{l_{\bar{\psi}}}{2}} - \left(\frac{\partial \bar{\theta}}{\partial \bar{r}} \right)_{\bar{R} - \frac{l_{\bar{r}}}{2}, \bar{\Psi} - \frac{l_{\bar{\psi}}}{2}} = 0 \quad (61)$$

$$\left(\frac{\partial \bar{\theta}}{\partial \bar{\psi}} \right)_{\bar{R} + \frac{l_{\bar{r}}}{2}, \bar{\Psi} - \frac{l_{\bar{\psi}}}{2}} - \left(\frac{\partial \bar{\theta}}{\partial \bar{\psi}} \right)_{\bar{R} + \frac{l_{\bar{r}}}{2}, \bar{\Psi} + \frac{l_{\bar{\psi}}}{2}} = 0 \quad (62)$$

$$\left(\frac{\partial \bar{\theta}}{\partial \bar{r}} \right)_{\bar{R} - \frac{l_{\bar{r}}}{2}, \bar{\Psi} + \frac{l_{\bar{\psi}}}{2}} - \left(\frac{\partial \bar{\theta}}{\partial \bar{r}} \right)_{\bar{R} + \frac{l_{\bar{r}}}{2}, \bar{\Psi} + \frac{l_{\bar{\psi}}}{2}} = 0 \quad (63)$$

$$\left(\frac{\partial \bar{\theta}}{\partial \bar{\psi}} \right)_{\bar{R} - \frac{l_{\bar{r}}}{2}, \bar{\Psi} + \frac{l_{\bar{\psi}}}{2}} - \left(\frac{\partial \bar{\theta}}{\partial \bar{\psi}} \right)_{\bar{R} - \frac{l_{\bar{r}}}{2}, \bar{\Psi} - \frac{l_{\bar{\psi}}}{2}} = 0 \quad (64)$$

in combination with these conditions, a node constraint for the density ratio, $\bar{\theta}(\bar{R}, \bar{\Psi}) = \bar{\theta}$, is imposed within in the micro-scale domain to close the problem.

2.2.3 Homogenization

In order to couple the effects of surface topography at the micro-scale with the macro-scale model, information is homogenized at the micro-scale and mapped to the numerical simulations at the macro-scale. The homogenized variables are functions of the six parameters defining the micro-scale model $(\bar{\theta}, \frac{\partial \bar{\theta}}{\partial \bar{r}}, \frac{\partial \bar{\theta}}{\partial \bar{\psi}}, \bar{H}, \bar{R}, \bar{\Psi})$. The homogenized density ratio at the macro-scale is the average value of

non-dimensional density ratio over the micro-scale domain as described by equation (65), resulting in the deviation of fluid pressure and load per unit area at the macro-scale.

$$\bar{\theta}^* \left(\bar{\theta}, \frac{\partial \bar{\theta}}{\partial \bar{R}}, \frac{\partial \bar{\theta}}{\partial \bar{\Psi}}, \bar{H}, \bar{R}, \bar{\Psi} \right) = \frac{\int_{\bar{R}-\frac{l_r}{2}}^{\bar{R}+\frac{l_r}{2}} \int_{\bar{\Psi}-\frac{l_\psi}{2}}^{\bar{\Psi}+\frac{l_\psi}{2}} \bar{\theta}(\bar{r}, \bar{\psi}) \, d\bar{\psi} d\bar{r}}{\int_{\bar{R}-\frac{l_r}{2}}^{\bar{R}+\frac{l_r}{2}} \int_{\bar{\Psi}-\frac{l_\psi}{2}}^{\bar{\Psi}+\frac{l_\psi}{2}} \bar{r}(\bar{r}, \bar{\psi}) \, d\bar{\psi} d\bar{r}} \quad (65)$$

The homogenized mass fluxes $\bar{Q}_{\bar{R}}$ and $\bar{Q}_{\bar{\Psi}}$, and shear stress $\bar{T}_{\bar{R}, \bar{\Psi}}$ in each coordinate direction are calculated in the subdomain from equations (66) (67) and (68) respectively,

$$\bar{Q}_{\bar{R}} \left(\bar{\theta}, \frac{\partial \bar{\theta}}{\partial \bar{R}}, \frac{\partial \bar{\theta}}{\partial \bar{\Psi}}, \bar{H}, \bar{R}, \bar{\Psi} \right) = \frac{\int_{\bar{\Psi}-\frac{l_\psi}{2}}^{\bar{\Psi}+\frac{l_\psi}{2}} \bar{q}_r \bar{r} \left(\bar{r} - \frac{l_r}{2}, \bar{\psi} \right) d\bar{\psi}}{\int_{\bar{\Psi}-\frac{l_\psi}{2}}^{\bar{\Psi}+\frac{l_\psi}{2}} \bar{r} \left(\bar{r} - \frac{l_r}{2}, \bar{\psi} \right) d\bar{\psi}} = \frac{1}{l_\psi} \int_{\bar{\Psi}-\frac{l_\psi}{2}}^{\bar{\Psi}+\frac{l_\psi}{2}} \bar{q}_r \left(\bar{r} - \frac{l_r}{2}, \bar{\psi} \right) d\bar{\psi} \quad (66)$$

$$\bar{Q}_{\bar{\Psi}} \left(\bar{\theta}, \frac{\partial \bar{\theta}}{\partial \bar{R}}, \frac{\partial \bar{\theta}}{\partial \bar{\Psi}}, \bar{H}, \bar{R}, \bar{\Psi} \right) = \frac{\int_{\bar{R}-\frac{l_r}{2}}^{\bar{R}+\frac{l_r}{2}} \bar{q}_\psi \left(\bar{r}, \bar{\psi} - \frac{l_\psi}{2} \right) d\bar{r}}{\int_{\bar{R}-\frac{l_r}{2}}^{\bar{R}+\frac{l_r}{2}} \left(\bar{r}, \bar{\psi} - \frac{l_\psi}{2} \right) d\bar{r}} = \frac{1}{l_r} \int_{\bar{R}-\frac{l_r}{2}}^{\bar{R}+\frac{l_r}{2}} \bar{q}_\psi \left(\bar{r}, \bar{\psi} - \frac{l_\psi}{2} \right) d\bar{r} \quad (67)$$

$$\bar{T}_{\bar{R}, \bar{\Psi}, 1,2} \left(\bar{\theta}, \frac{\partial \bar{\theta}}{\partial \bar{R}}, \frac{\partial \bar{\theta}}{\partial \bar{\Psi}}, \bar{H}, \bar{R}, \bar{\Psi} \right) = \frac{\int_{\bar{R}-\frac{l_r}{2}}^{\bar{R}+\frac{l_r}{2}} \int_{\bar{\Psi}-\frac{l_\psi}{2}}^{\bar{\Psi}+\frac{l_\psi}{2}} \bar{\tau}_{\bar{r}, \bar{\psi}, 1,2} \bar{r}(\bar{r}, \bar{\psi}) \, d\bar{\psi} d\bar{r}}{\int_{\bar{R}-\frac{l_r}{2}}^{\bar{R}+\frac{l_r}{2}} \int_{\bar{\Psi}-\frac{l_\psi}{2}}^{\bar{\Psi}+\frac{l_\psi}{2}} \bar{r}(\bar{r}, \bar{\psi}) \, d\bar{\psi} d\bar{r}} \quad (68)$$

where the boundaries $\left[\bar{R} - \frac{l_r}{2}, \bar{\Psi} \right]$ and $\left[\bar{r}, \bar{\psi} - \frac{l_\psi}{2} \right]$ are selected to calculate the homogenized mass flux arbitrarily from $\left[\bar{R} + \frac{l_r}{2}, \bar{\Psi} \right]$ and $\left[\bar{r}, \bar{\psi} + \frac{l_\psi}{2} \right]$. The micro-scale variables $\bar{Q}_{\bar{R}}$ and $\bar{Q}_{\bar{\Psi}}$ are dependent on the six macro-scale parameters and are used to determine the derivatives of terms required for the macro-scale model.

Variation of the density ratio in the micro-scale domain occurs due to the presence of surface topography, and an average pressure at the micro-scale is derived from a similar equation of which describe the load per unit area at the macro-scale model and from which the load capacity of the mechanical seal is calculated as described by equation (31).

2.2.4 Linearization

It is critical for the two-scale homogenization method to determine the partial derivative functions represented by the macro-scale lubrication model and given in value by corresponding micro-scale solutions. In this study the derivatives of mass fluxes with respect to the four variables $\bar{\theta}, \partial \bar{\theta} / \partial \bar{R}, \partial \bar{\theta} / \partial \bar{\Psi}, \bar{H}$ are approximated through a linearization method based on finite differencing. The mass fluxes are functions of the six variables $\bar{\theta}, \partial \bar{\theta} / \partial \bar{R}, \partial \bar{\theta} / \partial \bar{\Psi}, \bar{H}, \bar{R}, \bar{\Psi}$ at the macro-scale, of which the four derivatives needed are functions of the remaining two variables $\left(\bar{\theta}, \frac{\partial \bar{\theta}}{\partial \bar{R}}, \frac{\partial \bar{\theta}}{\partial \bar{\Psi}}, \bar{H} = f(\bar{R}, \bar{\Psi}) \right)$. The linearization scheme at each macro-scale node is therefore implemented using central finite difference of corresponding mass fluxes, i.e. (69), (70), (71).

$$f = f(x_i) \quad i = 1, \dots, m \quad (69)$$

$$x_j = x_j(x_k) \quad j = 1, \dots, n \quad k = n + 1, \dots, m \quad (70)$$

$$\frac{\partial f}{\partial x_j} = \frac{f(x_i + \Delta x_j \delta(j)) - f(x_i - \Delta x_j \delta(j))}{2\Delta x_j} \quad (71)$$

Here, f , is any function of the variables $x_i = (\bar{\theta}, \partial\bar{\theta}/\partial\bar{R}, \partial\bar{\theta}/\partial\bar{\Psi}, \bar{H}, \bar{R}, \bar{\Psi})$, this represents each macro-scale variable at every location and δ is the Dirichlet Delta function. The derivatives of the function f with respect to the variables $x_j = (\bar{\theta}, \partial\bar{\theta}/\partial\bar{R}, \partial\bar{\theta}/\partial\bar{\Psi}, \bar{H})$ are obtained by assuming a small perturbation of each variable. This perturbation is small enough to provide the linearized gradient of the function at that location (equation (72)),

$$\log_{10}(\Delta x_j) < \log_{10}(\max(x_j) - \min(x_j)) - \gamma \quad (72)$$

where the ranges of the variables x_j are chosen based on the solution to the single-scale problem at the macro-scale, which also forms the initial guess of the two-scale macro-scale solution procedure (see Section 3.2). The perturbation γ must be small enough to capture the gradient at any location, through the relaxation of these derivatives non-linearity is introduced at the macro-scale. The solution provided must be independent of the size of the perturbation. In this study $\gamma > 2$ is chosen for the stable convergence of the solutions which represents a less than 1% change over the range of values observed, a study of the sensitivity of γ is carried out accordingly.

3 Methods and materials

3.1 Material properties and operating conditions

The operating conditions and lubricant properties used to implement the numerical simulations undertaken in this study are defined in Table 1. To simplify the problem, the mechanical seal faces are made of steel with Young's modulus $E = 210$ GPa, Poisson's ratio $\nu = 0.3$ and such that they do not deform under the pressure experienced such that the longitudinal modulus M is calculated using equation (73),

$$M = \frac{(1 - \nu)E}{(1 + \nu)(1 - 2\nu)} \quad (73)$$

The asperity deformation δ can be approximated as the response to a 1D column of material under load as defined by equation (74),

$$\delta = kP \quad (74)$$

with the stiffness k given by equation (75),

$$k = \frac{t}{M} \quad (75)$$

where t is thickness of the steel surfaces. Then, equation (76) describes the relationship between asperity deformation and the minimum film thickness. Where if $c = 0.1$ say, then deformation is less than 10% of the minimum film thickness, i.e., it can be considered negligible in magnitude.

$$\delta < c H_0 \quad (76)$$

In the current work, $t = 10$ mm, and P is always less than 20 MPa which can be set as an upper limit. Therefore, a value of $H_{0\min} = 6.441$ μm is obtained for the minimum film thickness which does not lead to significantly asperity deformation according to the above equations. In the present work, the minimum film thickness used is greater than or equal to 9 μm such that the surface deformation can be negligible. The same conclusion that low-pressure introduces negligible asperity

deformation was drawn in by de Boer et al. ²⁵. Surface topography defined at the micro-scale are assumed to be evenly distributed across the whole face surface at the macro-scale, the roughness profile can therefore be considered isotropic as it remains constant over the entire contacting region.

Table 1. Operating Conditions and Geometry of a Mechanical Seal

Parameter	Value	Unit
Outer radius R_0	123	μm
Inner radius R_1	110	μm
Section angle Ψ_0	$\pi/4$	rad
Rotational speed ω	1000	rpm
Supply pressure P_1	3	MPa
Outlet pressure P_0	1	MPa
Cavitation pressure P_c	0	MPa
Waviness number n_w	8	-
Minimum film thickness H_0	9-15	μm
Scaling film thickness H_{00}	10	μm
Waviness amplitude A	10	μm
Topography amplitude A_t	2	μm
Lubricant density ρ_0	850	kg/m^3
Lubricant viscosity η	0.03	$\text{Pa}\cdot\text{s}$

3.2 Macro-scale solution procedure

Macro-scale solutions were calculated using the software Matlab (The MathWorks Inc., USA) in which the computational domain was discretized with uniform spacing of M mesh nodes in the radial direction and N in the angular direction. Discretization at the macro-scale is carried out for solving equation (13) using the finite difference scheme. At the macro-scale the discretization intervals in the radial and circumferential directions are defined in equation (77).

$$\begin{aligned}\Delta_{\bar{R}} &= \bar{R}_{i+1,j} - \bar{R}_{i,j} = \bar{R}_{i,j} - \bar{R}_{i-1,j} \\ \Delta_{\bar{\Psi}} &= \bar{\Psi}_{i,j+1} - \bar{\Psi}_{i,j} = \bar{\Psi}_{i,j} - \bar{\Psi}_{i,j-1} \\ i &= 1, \dots, M \quad j = 1, \dots, N\end{aligned}\tag{77}$$

A finite-difference derivative procedure shown in Figure 4 provides a possibility to develop a numerical partial differential equation (PDE) solver capable of dealing with the coupling of the micro- and macro- scale. In the first instance, solutions without surface topography were carried out to determine the initial guess for the case in which surface topography was considered. To do this, equation (8) including the effect of cavitation phenomenon was solved. The obtained solutions to density ratio and switch function were used as initial values for equation (13), through which the density ratio and switch function were updated. The iteration was repeated until convergence criteria of the density ratio was satisfied. The convergence criteria implemented in this study measured the difference in the maximum pressure obtained between two consecutive iterations and divided by the maximum pressure of the previous iteration. All computations were performed on an Intel(R) Core(TM) i5-7400 CPU with 4 Cores operating at 3.00 GHz.

Macro-scale solver

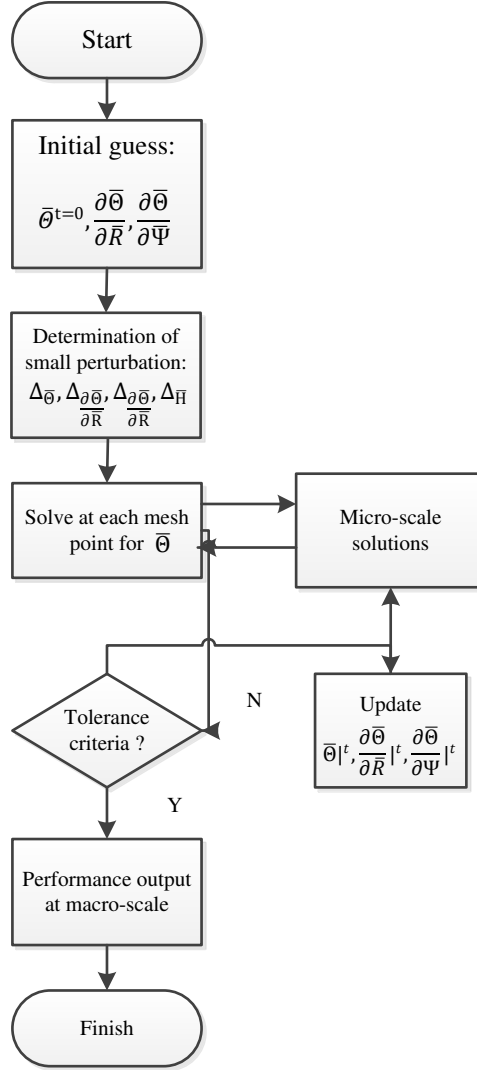


Figure 4 Flow Chart of the Finite-difference Derivative Procedure

In order to obtain the exact solutions of (13), the density ratio and corresponding gradients at each mesh node were updated using the Gauss-Seidel iteration scheme until the convergence criterion was achieved. The unknown variable $\bar{\theta}$ at each node was determined explicitly using the available nodal value of $\bar{\theta}$ at the neighboring nodes (equation (78)),

$$\bar{\theta}_{i,j}^t = \Phi \bar{\theta}_{i,j} + (1 - \Phi) \bar{\theta}_{i,j}^{t-1} \quad (78)$$

$$i = 1, \dots, M \quad j = 1, \dots, N$$

$$0 \leq \Phi \leq 1$$

where t is the iteration number, i and j denote the radial and angular direction, respectively. The variable Φ is an iteration factor which determines the degree of relaxation of the numerical scheme. A value of $\Phi = 0.1$ was chosen to improve the rate of convergence. The discretization representation of the equation (13) is described by the finite-difference method (equation (79)). Boundary conditions

were implemented at the macro-scale using finite differencing, see Appendix C for details.

$$\begin{aligned}
& \left. \frac{\partial(\overline{RQ}_{\overline{R}})}{\partial\overline{\Theta}} \right|_{i,j}^t \cdot \frac{\overline{\Theta}_{i+1,j} - \overline{\Theta}_{i-1,j}}{2\Delta_{\overline{R}}} + \left. \frac{\partial(\overline{RQ}_{\overline{R}})}{\partial\left(\frac{\partial\overline{\Theta}}{\partial\overline{R}}\right)} \right|_{i,j}^t \cdot \frac{\overline{\Theta}_{i+1,j} - 2\overline{\Theta}_{i,j} + \overline{\Theta}_{i-1,j}}{\Delta_{\overline{R}}^2} + \left. \frac{\partial(\overline{RQ}_{\overline{R}})}{\partial\left(\frac{\partial\overline{\Theta}}{\partial\overline{\Psi}}\right)} \right|_{i,j}^t \\
& \cdot \frac{\overline{\Theta}_{i+1,j+1} - \overline{\Theta}_{i+1,j-1} - \overline{\Theta}_{i-1,j+1} + \overline{\Theta}_{i-1,j-1}}{4\Delta_{\overline{R}}\Delta_{\overline{\Psi}}} + \left. \frac{\partial\overline{Q}_{\overline{\Psi}}}{\partial\overline{\Theta}} \right|_{i,j}^t \cdot \frac{\overline{\Theta}_{i,j+1} - \overline{\Theta}_{i,j-1}}{2\Delta_{\overline{\Psi}}} \\
& + \left. \frac{\partial\overline{Q}_{\overline{\Psi}}}{\partial\left(\frac{\partial\overline{\Theta}}{\partial\overline{R}}\right)} \right|_{i,j}^t \cdot \frac{\overline{\Theta}_{i+1,j+1} - \overline{\Theta}_{i+1,j-1} - \overline{\Theta}_{i-1,j+1} + \overline{\Theta}_{i-1,j-1}}{4\Delta_{\overline{R}}\Delta_{\overline{\Psi}}} + \left. \frac{\partial\overline{Q}_{\overline{\Psi}}}{\partial\left(\frac{\partial\overline{\Theta}}{\partial\overline{\Psi}}\right)} \right|_{i,j}^t \\
& \cdot \frac{\overline{\Theta}_{i,j+1} - 2\overline{\Theta}_{i,j} + \overline{\Theta}_{i,j-1}}{\Delta_{\overline{\Psi}}^2} + \left. \frac{\partial(\overline{RQ}_{\overline{R}})}{\partial\overline{H}} \right|_{i,j}^t \cdot \frac{\overline{H}_{i+1,j} - \overline{H}_{i-1,j}}{2\Delta_{\overline{R}}} + \left. \frac{\partial\overline{Q}_{\overline{\Psi}}}{\partial\overline{H}} \right|_{i,j}^t \\
& \cdot \frac{\overline{H}_{i,j+1} - \overline{H}_{i,j-1}}{2\Delta_{\overline{\Psi}}} = 0 \\
& i = 2, \dots, M-1 \quad j = 2, \dots, N-1
\end{aligned} \tag{79}$$

In equation (79) the derivatives of mass fluxes in the two directions were functions of six parameters

$\overline{\Theta}_{i,j}^t, \left. \frac{\partial\overline{\Theta}}{\partial\overline{R}} \right|_{i,j}^t, \left. \frac{\partial\overline{\Theta}}{\partial\overline{\Psi}} \right|_{i,j}^t, \overline{H}_{i,j}, \overline{R}_{i,j}, \overline{\Psi}_{i,j}$ (equation (80)).

$$\begin{aligned}
& \left. \frac{\partial(\overline{RQ}_{\overline{R}})}{\partial\overline{\Theta}} \right|_{i,j}^t, \left. \frac{\partial(\overline{RQ}_{\overline{R}})}{\partial\left(\frac{\partial\overline{\Theta}}{\partial\overline{R}}\right)} \right|_{i,j}^t, \left. \frac{\partial(\overline{RQ}_{\overline{R}})}{\partial\left(\frac{\partial\overline{\Theta}}{\partial\overline{\Psi}}\right)} \right|_{i,j}^t, \left. \frac{\partial(\overline{RQ}_{\overline{R}})}{\partial\overline{H}} \right|_{i,j}^t, \left. \frac{\partial\overline{Q}_{\overline{\Psi}}}{\partial\overline{\Theta}} \right|_{i,j}^t, \left. \frac{\partial\overline{Q}_{\overline{\Psi}}}{\partial\left(\frac{\partial\overline{\Theta}}{\partial\overline{R}}\right)} \right|_{i,j}^t, \left. \frac{\partial\overline{Q}_{\overline{\Psi}}}{\partial\left(\frac{\partial\overline{\Theta}}{\partial\overline{\Psi}}\right)} \right|_{i,j}^t, \left. \frac{\partial\overline{Q}_{\overline{\Psi}}}{\partial\overline{H}} \right|_{i,j}^t \\
& = f\left(\overline{\Theta}_{i,j}^t, \left. \frac{\partial\overline{\Theta}}{\partial\overline{R}} \right|_{i,j}^t, \left. \frac{\partial\overline{\Theta}}{\partial\overline{\Psi}} \right|_{i,j}^t, \overline{H}_{i,j}, \overline{R}_{i,j}, \overline{\Psi}_{i,j}\right) \\
& i = 1, \dots, M \quad j = 1, \dots, N
\end{aligned} \tag{80}$$

A sparse matrix was constructed using this process and consisted of coefficients determined by derivatives of mass fluxes derived at the micro-scale. The resulting system of equation was then solved using the iterative Gauss-Seidel method. In each iteration, the unknown variables $\overline{\Theta}$ and \overline{G} at each node were updated based on previous estimations as described by equation (32) and (33). Subsequently, gradients of density ratio at each node were updated based on the current estimation of the density ratio. The current gradients of the density ratio were calculated by using a central difference for internal nodes, a forward difference for bottom and right sides and a backward difference method for top and left sides of the subdomain. As the iteration number increases, $\overline{\Theta}_{i,j}^t$ tends to $\overline{\Theta}_{i,j}^{t-1}$, i.e. (81),

$$\lim_{t \rightarrow \infty} \left(\max_{i,j} |\overline{\Theta}_{i,j}^t - \overline{\Theta}_{i,j}^{t-1}| \right) < 10^{-3} \tag{81}$$

where 10^{-3} is the tolerance of the macro-scale solver. See Appendix C for more details of the macro-scale finite differencing solution procedure

3.3 Micro-scale solution procedure

Micro-scale solutions included in the macro-scale solution were parameterized by the variables of the

macro-scale model $(\bar{\Theta}, \partial\bar{\Theta}/\partial\bar{R}, \partial\bar{\Theta}/\partial\bar{\Psi}, \bar{H}, \bar{R}, \bar{\Psi})$. For solving equation (42), discretization at the micro-scale is presented in this section. First, the finite difference form of equation (42) is given, and subsequently the boundary conditions are developed for each boundary of the domain. Then the iterative equations which are written in the difference form for each micro-scale node are outlined. The micro-scale solution procedure is illustrated in Figure 5.

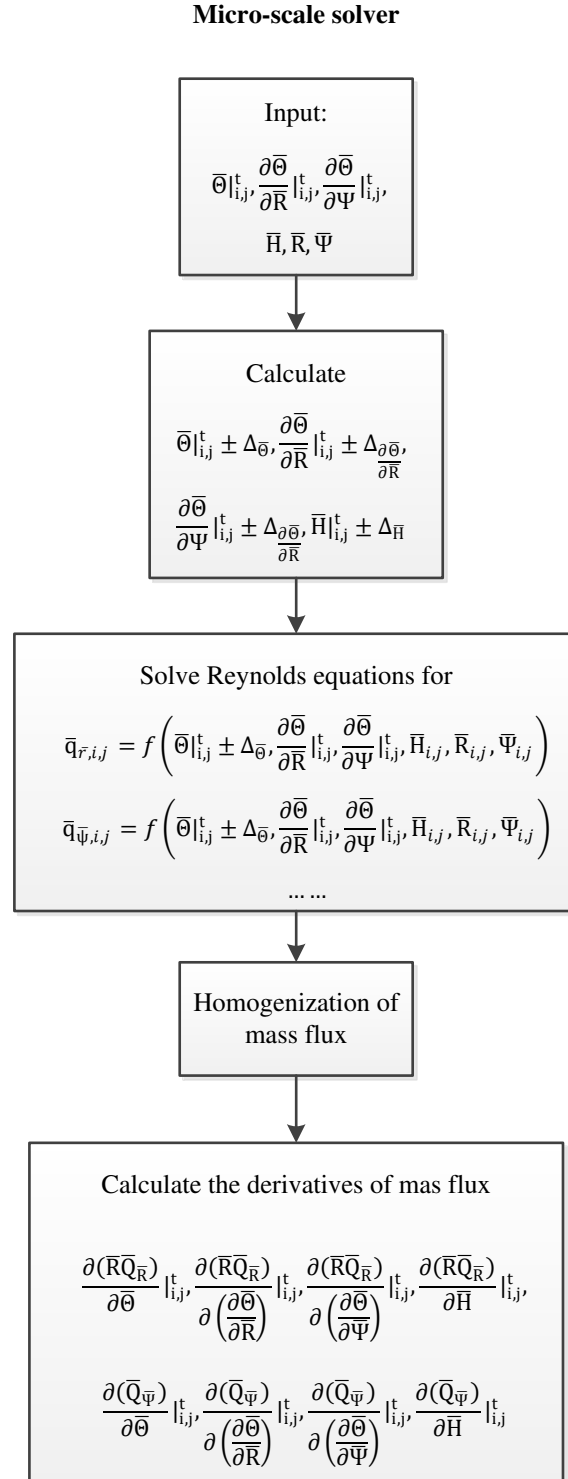


Figure 5 Flow Chart of Micro-scale Solution

At the micro-scale, the discretization intervals at the radial and circumferential direction were defined using uniform spacing, where there were m total mesh nodes in the radial direction and n in the circumferential direction (equation (82)),

$$\begin{aligned}\Delta_{\bar{r}} &= \bar{r}_{i+1,j} - \bar{r}_{i,j} = \bar{r}_{i,j} - \bar{r}_{i-1,j} \\ \Delta_{\bar{\psi}} &= \bar{\psi}_{i,j+1} - \bar{\psi}_{i,j} = \bar{\psi}_{i,j} - \bar{\psi}_{i,j-1} \\ i &= 1, \dots, m \quad j = 1, \dots, n\end{aligned}\quad (82)$$

the density ratio was solved using a Gauss-Seidel iteration method with the similar convergence criteria as the macro-scale solver. The micro-scale density ratio $\bar{\theta}$ was updated at each iteration (t) of the micro-scale solution procedure according to equation (83),

$$\begin{aligned}\bar{\theta}_{i,j}^t &= \varphi \bar{\theta}_{i,j} + (1 - \varphi) \bar{\theta}_{i,j}^{t-1} \\ i &= 1, \dots, m \quad j = 1, \dots, n \\ 0 &\leq \varphi \leq 1\end{aligned}\quad (83)$$

where φ is an additional iteration factor which determines the degree of relaxation of the numerical scheme at the micro-scale, a value of $\varphi = 0.1$ was chosen for this study for stability purposes. The discretized finite difference of equation (42) was written as equation (84),

$$\begin{aligned}\bar{\theta}_{i+1,j} &\left(\bar{g}_{i,j}^t \frac{\bar{r}_{i+1/2,j} \bar{h}_{i+1/2,j}^3}{\Delta_{\bar{r}}^2} \right) + \bar{\theta}_{i-1,j} \left(\bar{g}_{i,j}^t \frac{\bar{r}_{i-1/2,j} \bar{h}_{i-1/2,j}^3}{\Delta_{\bar{r}}^2} \right) \\ &+ \bar{\theta}_{i,j+1} \left(\bar{g}_{i,j}^t \frac{\bar{h}_{i,j+1/2}^3}{\bar{r}_{i,j} \Delta_{\bar{\psi}}^2} + (1 - \lambda \bar{g}_{i,j}^t) \bar{h}_{i,j+1} \right) \\ &+ \bar{\theta}_{i,j-1} \left(\bar{g}_{i,j}^t \frac{\bar{h}_{i,j-1/2}^3}{\bar{r}_{i,j} \Delta_{\bar{\psi}}^2} + (1 - \lambda \bar{g}_{i,j}^t) \bar{h}_{i,j-1} \right) \\ &- \bar{\theta}_{i,j} \left(\bar{g}_{i,j}^t \frac{\bar{r}_{i+1/2,j} \bar{h}_{i+1/2,j}^3 + \bar{r}_{i-1/2,j} \bar{h}_{i-1/2,j}^3}{\Delta_{\bar{r}}^2} + \bar{g}_{i,j}^t \frac{\bar{h}_{i,j+1/2}^3 + \bar{h}_{i,j-1/2}^3}{\bar{r}_{i,j} \Delta_{\bar{\psi}}^2} \right. \\ &\left. + (1 - \lambda \bar{g}_{i,j}^t) 2\bar{h}_{i,j} \right) = \lambda \bar{g}_{i,j}^t \bar{r}_{i,j} \frac{\bar{\theta}_{i,j+1}^{t-1} \bar{h}_{i,j+1} - \bar{\theta}_{i,j-1}^{t-1} \bar{h}_{i,j-1}}{2\Delta_{\bar{\psi}}}\end{aligned}\quad (84)$$

$$i = 2, \dots, m - 1 \quad j = 2, \dots, n - 1$$

where the discrete form of the micro-scale switch function $\bar{g}_{i,j}^t$ was defined at each solution time by (85). Boundary conditions, constraints, were implemented at the micro-scale by finite differencing as detailed in Appendix D.

$$\begin{aligned}\bar{g}_{i,j}^t &= \begin{cases} \frac{1}{\lambda} & \bar{\theta}_{i,j}^t > \frac{1}{\lambda} \\ 0 & \bar{\theta}_{i,j}^t \leq \frac{1}{\lambda} \end{cases} \\ i &= 1, \dots, m \quad j = 1, \dots, n\end{aligned}\quad (85)$$

Subsequently, the calculation of the micro-scale mass fluxes in each of the coordinate directions was

undertaken such that the homogenized mass fluxes were determined to obtain its corresponding derivatives. As the iteration number increased, $\bar{\theta}_{i,j}^t$ tended to $\bar{\theta}_{i,j}^{t-1}$, i.e. equation (86),

$$\lim_{t \rightarrow \infty} \left(\max_{i,j} |\bar{\theta}_{i,j}^t - \bar{\theta}_{i,j}^{t-1}| \right) < 10^{-3} \quad (86)$$

where 10^{-3} is the tolerance of the micro-scale solver. The assessments of gradient and integral quantities at the micro-scale were also achieved using finite differencing, see Appendix D for the micro-scale finite differencing solution procedure.

4 Results and discussion

4.1 Model validation

Model validation for the two-scale method derived was carried out through parameter sensitivity and mesh convergence of simulations at both scales. The parameters affecting the accuracy and convergence of the simulation process for the given operating conditions were the bulk modulus β , the linearization factor γ , and the mesh size.

4.1.1 Sensitivity analysis

All macro-scale objectives in this study are presented in terms of the fluid bulk modulus β and linearization parameter γ , hence the evaluation of the sensitivity of the accuracy of the model solutions to these parameters is needed. For this purpose, a sensitivity study was performed by varying β and γ and assessing the tolerance error, $\text{Error} = \max_{i,j} |\bar{\theta}_{i,j}^t - \bar{\theta}_{i,j}^{t-1}| / \max_{i,j} (\bar{\theta}_{i,j}^0)$, for fixed separation of scales $\epsilon = 1/2^{-4}$ and $\bar{A}_t = 0.2$.

The possibility of numerical instabilities for particular values of β was reported by Elrod and Adams²⁷. The stability of the solution presented is shown in Figure 6 where all three cases investigated converged to the same value. The corresponding values of load carrying capacity obtained are listed in Table 2. Varying the value of β from 1 to 100 GPa only slightly changed the values of the load carrying capacity such that the value of β used did not affect the accuracy of predictions. For the consideration of stability of solutions, a value of $\beta = 1$ GPa was adopted in the remainder of the investigation.

Table 2. Load Carrying Capacity for Different Values of Bulk modulus β

Bulk modulus β (GPa)	Non-dimensional parameter λ	Non-dimensional load carrying capacity \bar{L}
$\beta = 1$	$\lambda = 1.426$	$\bar{L} = 1.378 \times 10^{-4}$
$\beta = 10$	$\lambda = 0.1426$	$\bar{L} = 1.361 \times 10^{-4}$
$\beta = 100$	$\lambda = 0.01426$	$\bar{L} = 1.360 \times 10^{-4}$

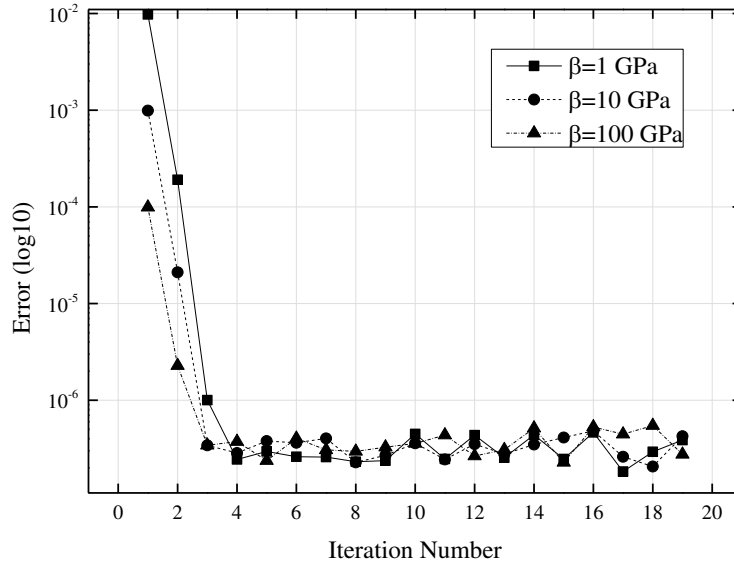


Figure 6 Sensitivity Analysis of β for $\gamma = 2$

The influence of γ on the accuracy of simulations is shown in Figure 7 where three cases were considered. The value of β adopted was obtained from the previous study to ensure the stable convergence for different operating conditions. A high accuracy where the tolerance error converged to a lower value was observed when $\gamma = 2$. A high value up to $\gamma = 4$ does not present any additional accuracy benefit since the size of the error produced was very low ($\sim 10^{-6}$ compared to $\sim 10^{-4}$). Therefore, a value of $\gamma = 2$ was used in the remainder of this study.

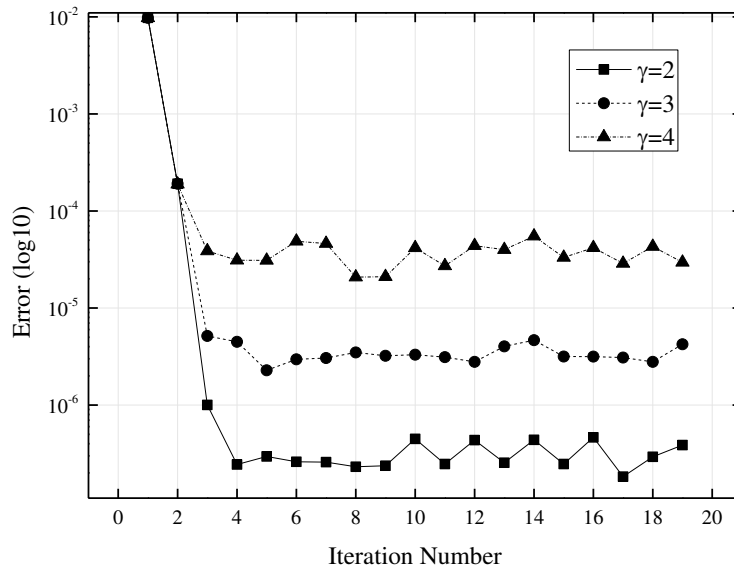


Figure 7 Sensitivity Analysis of γ for $\beta = 1$ GPa

4.1.2 Mesh convergence at both scales

The mesh number, which is the level of geometrical discretization specified in the coordinate directions, is of high importance due to the precision of numerical simulations relying on the number of mesh elements. A mesh convergence for both micro and macro-scale simulations was therefore performed to choose an appropriate discretization. In order to ensure convergence, $\beta = 1$ GPa and $\gamma = 2$ were used as mentioned in previous section.

The mesh number required for the micro-scale model was determined based on homogenized pressure (load per unit area) produced in these simulations. The relative percentage error in the homogenized pressure against the homogenized pressure with the largest number of mesh nodes (80×80) $e_{\bar{P}^*} = |\bar{P}_{M \times N}^* - \bar{P}_{80 \times 80}^*| / \bar{P}_{80 \times 80}^* \times 100\%$ was plotted in Figure 8 for the separation of scale $\epsilon = 2^{-4}$, and the non-dimensional topography amplitude $\bar{A}_t = 0.2$. In this simulation, the following macro-scale values were assigned: density ratio $\bar{\Theta} = 0.7099$, the density ratio gradients $d\bar{\Theta}/d\bar{R} = 0.0053$, $d\bar{\Theta}/d\bar{\Psi} = -0.0041$, and film thickness $\bar{H} = 0.7006$. It was shown that the change in the percentage error was reduced as the mesh number increased describing convergence of the solution. In this study 30×30 was chosen because it could accurately capture the micro-scale phenomenon at moderate computational cost.

Mesh convergence at the macro-scale was undertaken to determine the number of mesh nodes required for predicting accurate results. The relative percentage error in the non-dimensional load-carrying capacity \bar{L} against the non-dimensional load-carrying capacity with the largest number of mesh nodes ($e_{\bar{L}} = |\bar{L}_{M \times N} - \bar{L}_{80 \times 80}| / \bar{L}_{80 \times 80} \times 100\%$) was evaluated by varying the number of mesh nodes used. As example simulations, the non-dimensional minimum film thickness was taken as unit ($\bar{H}_0 = 1$). The convergence of mesh at the macro-scale was achieved when mesh number 50×50 was used (Figure 9). In this study, the mesh number of 40×40 was used for all macro-scale simulations as the computational cost was greatly reduced compared to more refined meshes and this resolution maintained accurate results independent of the level of discretization.

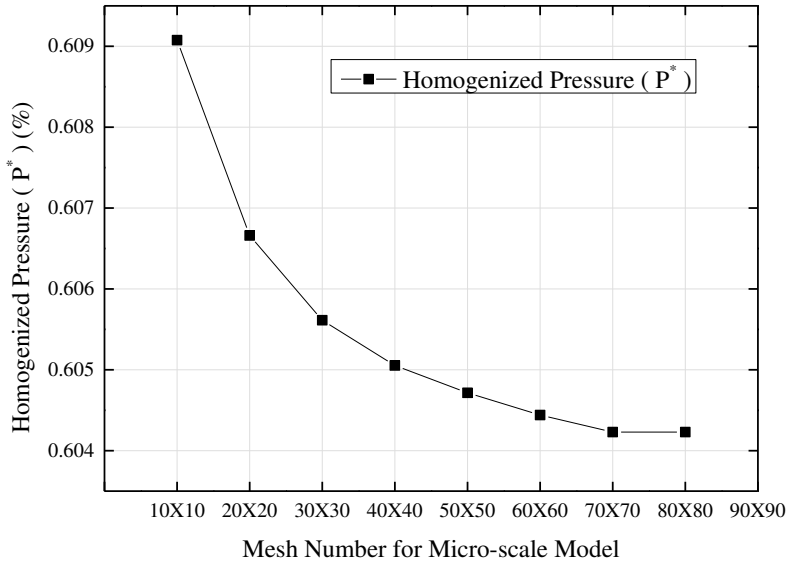


Figure 8 Mesh Convergence at Micro-scale

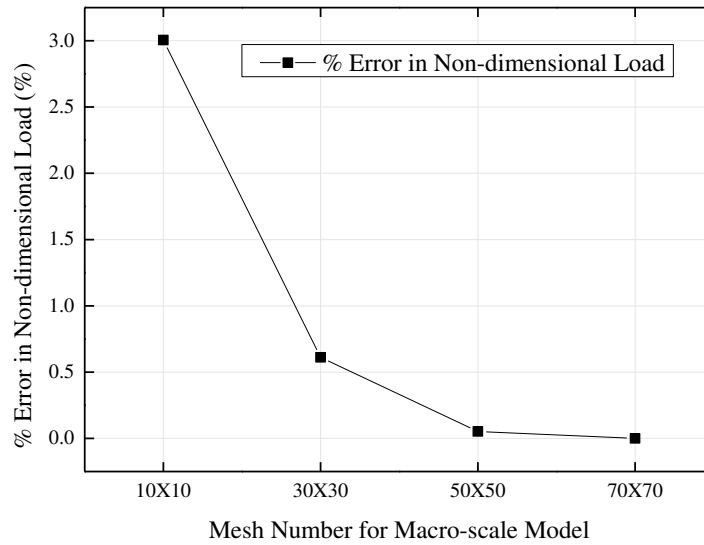


Figure 9 Mesh Convergence at Macro-scale

4.1.3 Validation of scale separation

The general form of macro-scale model based on mass-flux derivatives was validated by comparing the non-dimensional load carrying capacity predicted by the two-scale model and that by the single-scale Elrod model for a case without surface topography ($\bar{A}_t = 0$) at the micro-scale. To achieve this, the mesh size at the macro-scale was varied until results converged for the separation of scales $\epsilon = 1/2^4$. The difference between the results predicted by the two-scale model and the single model was very small as shown in Figure 10. The relative percentage error in the non-dimensional load carrying capacity predicted by the two models was $< 5\%$ for all cases, and the same percentage error (to within 3 significant figures) was obtained when the mesh number 50×50 was adopted. Therefore the two-scale model is justified as a valid approach for capturing the effects of surface topography on the mechanical seal since in the case without topography the model predictions are identical to that of the single-scale model. When surface topography is included, deviation from the single-scale solution is described in the two-scale model by variance in mass flux derivatives using homogenized micro-scale data compared to that given by the single-scale derivatives.

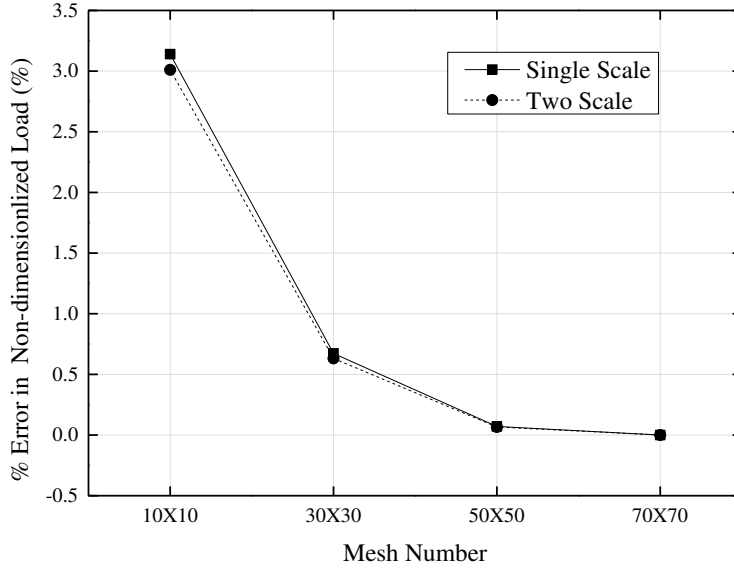


Figure 10 The Comparison of Non-dimensional Load Carrying Capacity Predicted by Single and Two Scale Model, Error = $|\bar{L}_{M \times N} - \bar{L}_{70 \times 70}| / \bar{L}_{70 \times 70} \times 100\%$

4.2 Micro-scale solutions

Micro-scale distributions of the film thickness (\bar{h}) density ratio ($\bar{\theta}$) and distribution of fluid pressure are given in Figure 11, Figure 12, and Figure 13 and respectively. In this section, figures are presented under the Cartesian coordinates (\bar{x}, \bar{y}) which the micro-scale Polar coordinates $(\bar{r}, \bar{\psi})$ are transformed to for visualization purposes only. These distributions corresponded to a micro-scale solution where the cell density ratio $\bar{\theta} = 0.7013$, the density ratio gradients $d\bar{\theta}/d\bar{r} = 2.0$, $d\bar{\theta}/d\bar{\psi} = 0$, film thickness $\bar{H} = 0.9996$, and the topography amplitude $\bar{A}_t = 0.2$. All results obtained here corresponded to the scale separation of $\epsilon = 2^{-4}$.

Figure 11 showed the variation and contour of film thickness modeled by equation (48) where periodicity on opposing boundaries existed so as to satisfy the requirement of two-scale method. From Figure 12 it was seen that density ratio in the micro-scale domain was not constant through the film out the domain due to the existence of surface topography and use of lubrication theory to describe fluid flow which was driven through the film= by entrainment from the moving surface and the pressure boundary conditions. Fluid pressure shown in Figure 13 was calculated using equation (44). Near-periodicity of fluid pressure and density ratio on the opposing boundaries were obtained due to the constant shift in magnitude applied between the boundaries of the micro-scale domain. The homogenized mass fluxes were calculated from these solutions obtained at the micro-scale and were represented at the macro-scale using the corresponding mass flux derivatives.

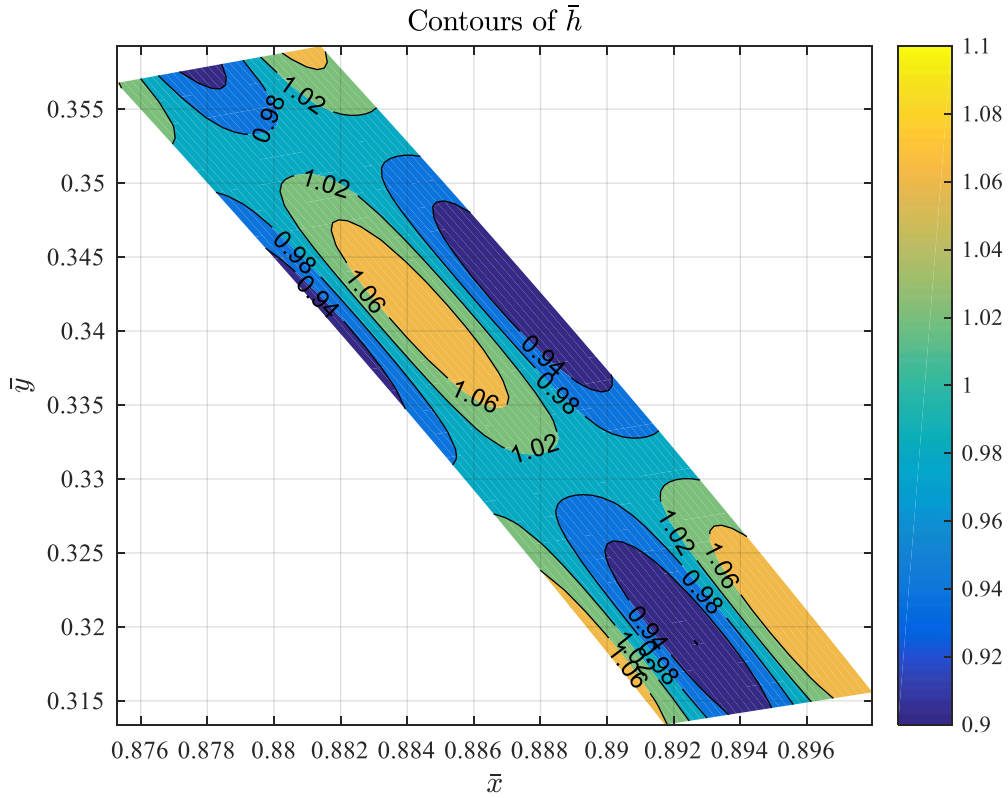


Figure 11 Film Thickness at the Micro-scale

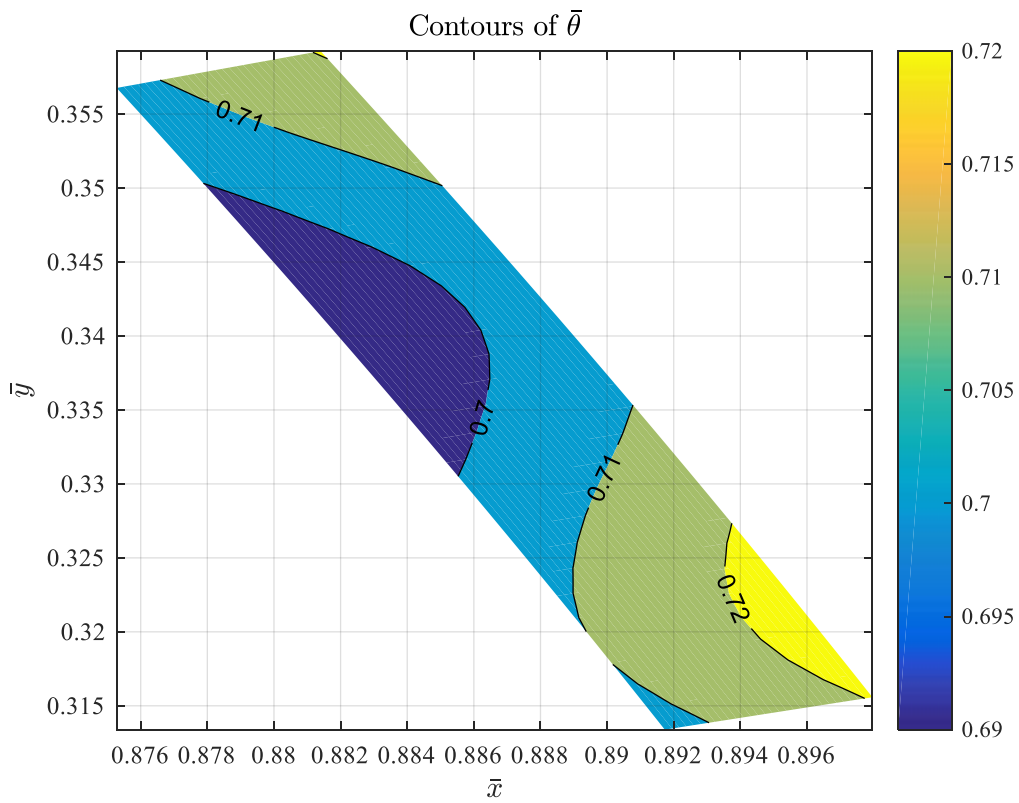


Figure 12 Density Ratio at the Micro-scale

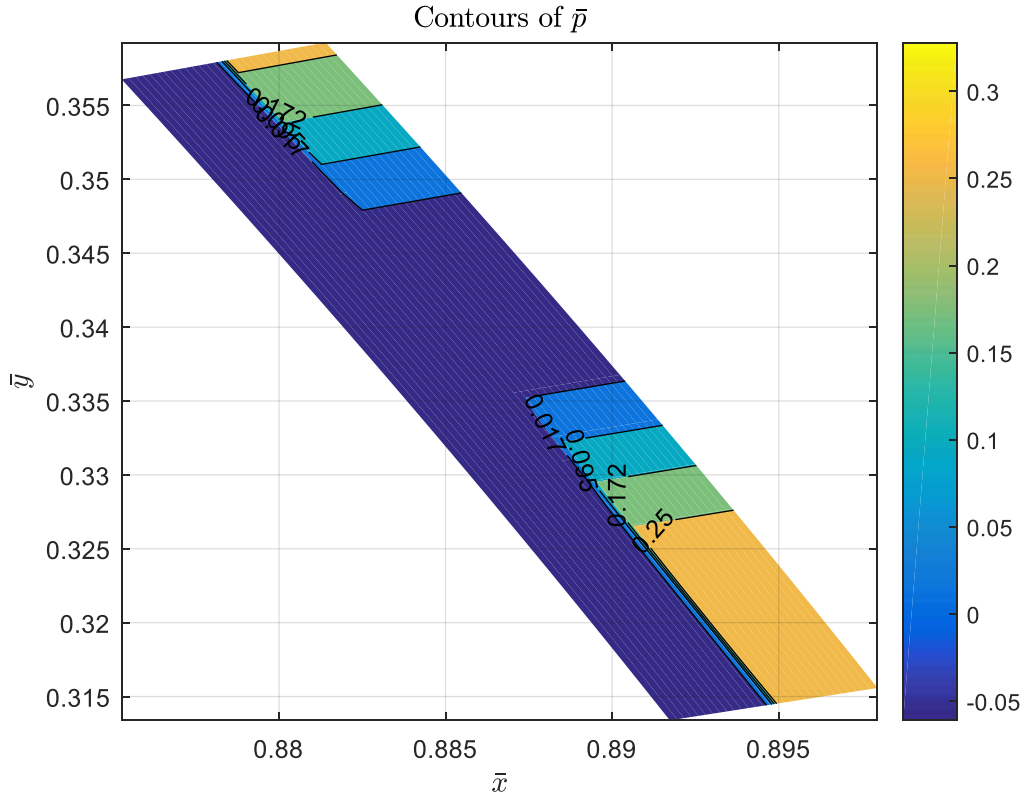


Figure 13 Pressure Distribution at the Micro-scale

4.3 Macro-scale solutions

4.3.1 Effect of the micro-scale topography amplitude \bar{A}_t

In this section results of both the single- and two-scale models are presented to show the difference introduced by surface topography in the lubricated domain. Macro-scale Polar coordinates $(\bar{R}, \bar{\Psi})$ were transformed to Cartesian coordinates in the following analysis (\bar{X}, \bar{Y}) for visualization purposes only. Figure 14 illustrates contours of fluid pressure obtained using single-scale model. Figure 15 shows contours of the difference in pressure derived between single-scale and two-scale model for $\epsilon = 2^{-4}$, $\bar{A}_t = 0.2$. Fluid pressure was produced through the domain by entrainment from the moving seal face and the pressure jump in the radial direction. However there were differences in the pressure distributions at the macro-scale when surface topographies were considered.

Figure 15 Contour of Pressure Difference Derived between Single-scale and Two-scale, \bar{P}_{two} is Fluid Pressure Obtained Using Two-scale Homogenization Method

To demonstrate the tribological performance of a mechanical seal, a range of topography amplitudes were specified and the resulting load-carrying capacity, friction force and friction coefficient were evaluated. A series of numerical simulations were presented by incrementing the topography amplitude in steps of 0.05 from $\bar{A}_t = 0$ to $\bar{A}_t = 0.25$ to investigate the change in performance of a mechanical seal. For each value of the topography amplitude the micro-scale problem was solved and then coupled into the macro-scale model. The value of \bar{H}_0 was specified to 1 and the fixed scale separation was specified as $\epsilon = 2^{-4}$.

Figure 16 shows the percentage change in non-dimensional macro-scale load-carrying capacity against the case where topography amplitude was zero, i.e., $C_L = \frac{|\bar{L}_{\bar{A}_t} - \bar{L}_{\bar{A}_t=0}|}{\bar{L}_{\bar{A}_t=0}} \times 100\%$, indicating that increasing the size of surface topography corresponded to an increase in non-dimensional macro-scale load-carrying capacity. Figure 17 presented the variation of percentage error in friction coefficient against the case where topography amplitude was zero, i.e., $C_\mu = \frac{|\mu_{\bar{A}_t} - \mu_{\bar{A}_t=0}|}{|\mu_{\bar{A}_t=0}|} \times 100\%$, describing the magnitude of friction coefficient of both rotor and stator faces. It was seen that increasing the value of topography amplitude tended to reduce the magnitude of friction coefficient of both the stator and rotor faces in the radial direction but also led to an increase in the magnitude of friction coefficient of both stator and rotor face in the angular direction. Compared to the smooth assumption where $\bar{A}_t = 0$, the presence of surface topography indeed could improve tribological performance for a mechanical seal in terms of increasing load-carrying capacity and reducing friction coefficient in the radial direction.

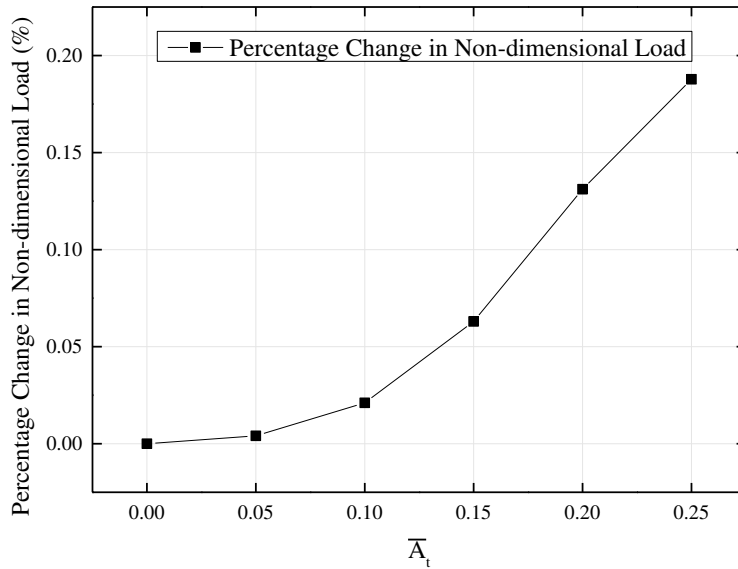


Figure 16 Effect of Topography Amplitude on the Load Carrying Capacity

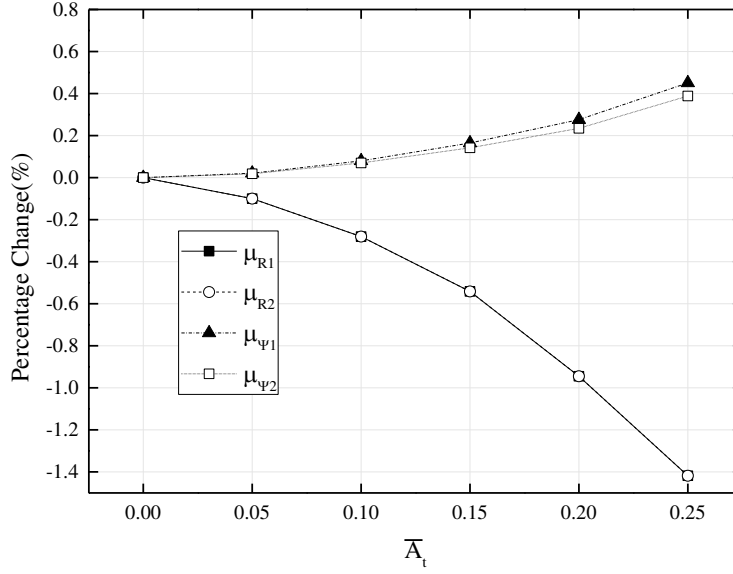


Figure 17 Effect of Topography Amplitude on Friction Coefficient, (1) μ_{R1} : Friction Coefficient of Stator Face at the Radial Direction, (2) μ_{R2} : Friction Coefficient of Rotor Face at the Radial Direction, (3) $\mu_{\psi1}$: Friction Coefficient of Stator Face at the Angular Direction, (4) $\mu_{\psi2}$: Friction Coefficient of Rotor Face at the Angular Direction

4.3.2 Effect of the separation of scales ϵ

If the separation of scales is small enough, the two-scale solution gives the exact same result (87) as the smooth case without topography. To assess the validation of the macro-scale model, the effect of the scale separation ϵ on the non-dimensional load-carrying capacity was investigated for topography amplitude $\bar{A}_t = 0.2$ using the percentage error e defined as

$$\text{equation/ (87).} e = \frac{|L_{\epsilon} - L_{\epsilon=2^{-6}}|}{L_{\epsilon=2^{-6}}} \times 100\%$$

Figure 18 shows that the percentage difference of non-dimensional load-carrying capacity obtained using the two-scale method converged to the value of smooth case when the scale separation tended toward zero. The curve presented was similar to that obtained by Almqvist¹⁸ thus justifying the result of the model prediction again. The trend shown also indicated that increasing the separation of scales also increased the load carried within the contact for the same operating conditions. The variation of percentage change in friction coefficient against the largest friction coefficient with scale separation $\epsilon = 1/2^{-6}$ were presented in Figure 19, showing that reducing the separation of scales increased the friction coefficient of both the rotor and stator faces simultaneously. It can be inferred from both figures that a larger size of surface topography is beneficial to improving tribological performance within the parameter bounds investigated.

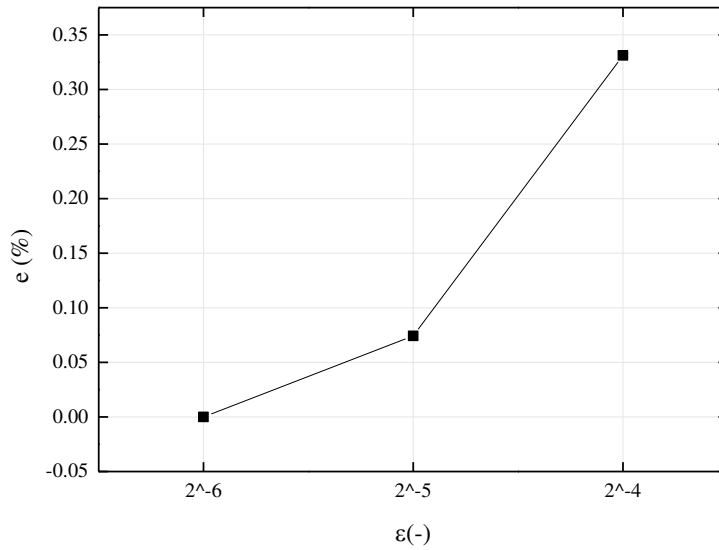


Figure 18 Variation of the % Difference Non-dimensional Load Carrying Capacity e with the Scale Separation ϵ

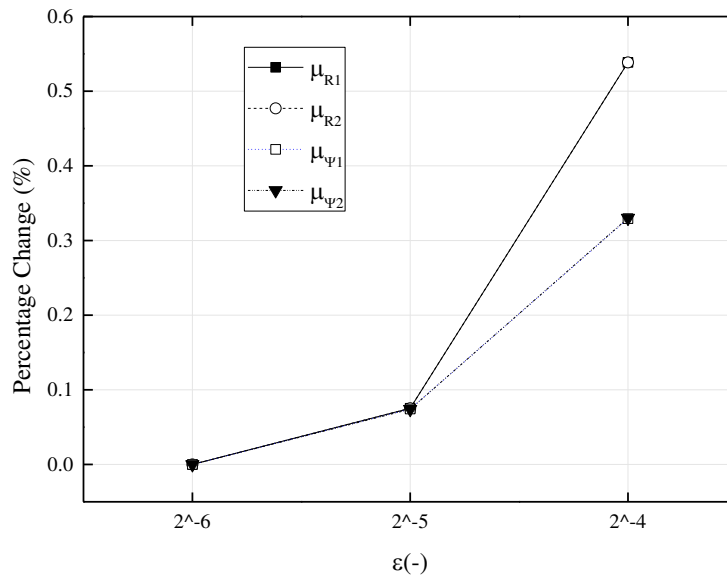


Figure 19 Variation of the Percentage Change of Friction Coefficient with the Scale Separation ϵ

4.3.3 Stribeck curve analysis

To investigate the hydrodynamic influence predicted by the two-scale homogenization method in the fluid film, the modified Sommerfeld number S was varied to obtain a Stribeck curve for the seal. The value of S shown in Figure 20 was produced by varying film thickness from $9 \mu\text{m}$ to $15\mu\text{m}$ with and without surface topography. The friction coefficient obtained at the macro-scale was subsequently plotted as a function of S as shown in Figure 21 where both cases were considered, i.e., (1) with surface topography, (2) without surface topography.

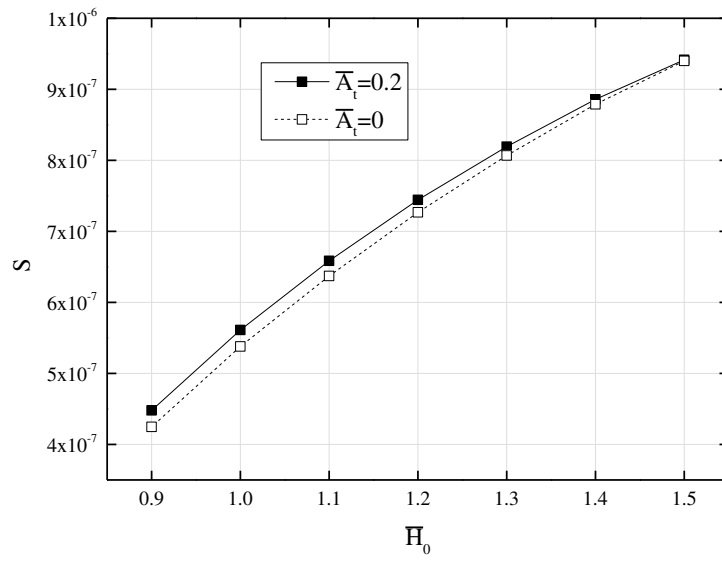
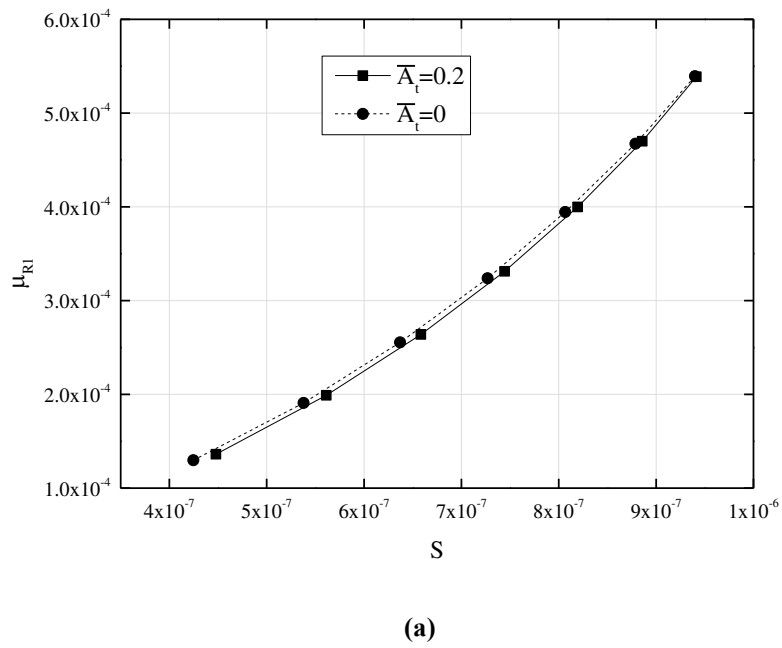
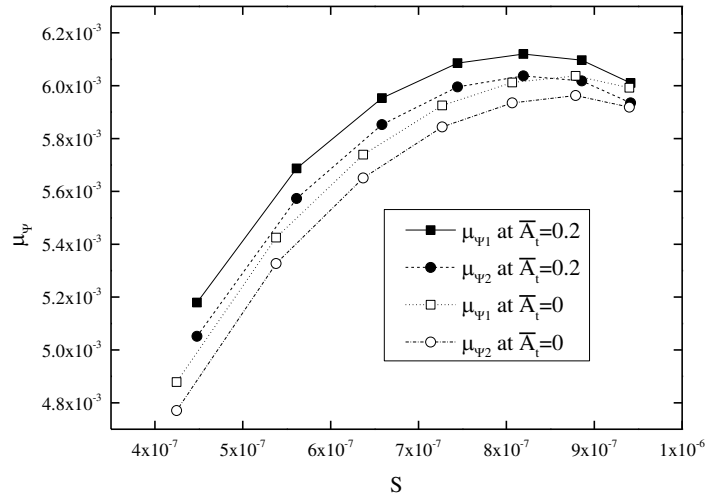


Figure 20 Variation of Modified Sommerfeld S Number with Film Thickness





(b)

Figure 21 Stribeck Curve with and without Surface Topography, (a) Variation of Friction Coefficient μ_{R1} , (b) Variation of Friction Coefficient μ_{ψ_1} , μ_{ψ_2}

This type of illustration showed an overall view of the variation of friction coefficient for the range of the hydrodynamic lubrication regime. Within this regime, the hydrodynamic lift was large enough to separate the two lubricated surfaces and the friction coefficient of the stator face in the radial direction increased as the parameter S also increased, see Figure 21(a). The trends of friction coefficients in the angular direction were illustrated in Figure 21(b). The result presented by multi-scale model resulted in a prediction of the friction coefficient value with a satisfactory accuracy. The general shape of the friction coefficient curves from the stator face at the radial direction obtained were well reproduced in this study compared to the well-established single-scale solution [add citation here]. Overall, the result of the Stribeck analysis is clear. For the hydrodynamic regime, when surface topography is included the load carrying capacity is increased and the frictional forces are reduced for the same operating conditions.

4.3.4 Effect of the macro-scale surface waviness \bar{A}

To demonstrate the effect of the macro-scale variation in surface profile, the non-dimensional macro-scale surface waviness \bar{A} is varied over a range of 0.3 to 0.5, with the results in the remainder of Section 4.3 being at a value of $\bar{A} = 1$. Figure 22 and Figure 23 respectively show the effect of varying the non-dimensional topography amplitude \bar{A}_t and separation of scales ϵ along with the surface waviness on the total load carried by the mechanical seal. Both figures show that the change in load caused by variation in the macro-scale surface waviness the macro-scale variation in surface profile, the non-dimensional macro-scale surface waviness \bar{A} is significantly larger than the change caused by increasing the micro-scale variables \bar{A}_t and ϵ . The deviation generated by including the two-scale model cannot be described by the variation in the macro-scale profile alone without reaching a computational limit on the resolution of the discrete domain. Results obtained inclusive of the micro-scale cannot be obtained in any other way and cause significant changes in the tribological performance of the mechanical seal in terms of both load and friction.

Figure 22 The influence of the non-dimensional macro-scale amplitude \bar{A} on the percentage error of the non-dimensional load carrying capacity $E_L = (\bar{L}_A - \bar{L}_{\bar{A}=0.3})/\bar{L}_{\bar{A}=0.3} \times 100\%$ for different non-dimensional topography amplitude \bar{A}_t

$$(\bar{L}_A - \bar{L}_{\bar{A}=0.3})/\bar{L}_{\bar{A}=0.3}$$

5 Conclusion

Surface topography may contribute to an increase in pressure where hydrodynamic lubrication prevails thus improving load-carrying capacity and reducing friction. From an engineering application prospect, it is of interest to improve the tribological performance by altering the configurations of surface topography. Evaluation of the influence of surface topography addresses a problem associated with computational cost as fine meshes over the discrete domain are required to accurately describe the configuration of surface features in numerical simulations. Moreover, earlier studies towards such goals were restricted to Cartesian coordinate systems, which are not applicable for some rotational devices and model need adapting accordingly.

The scope of this research was to develop a two-scale model for hydrodynamic lubrication in relation to mechanical seals in which the effects of surface topography are included. This work furthers the homogenization approach developed for two-scale lubrication based on the HMM published over the last few years [2]. The model implements the Elrod cavitation algorithm [3] over two disparate scales for the first time, includes a new derivative-coupling procedure for linking simulations at different scales, includes the development of a novel solution procedure and solver based on finite-differencing, and is implemented using a cylindrical Polar coordinate system.

In the present study a novel finite-difference derivative scheme was presented and applied to mechanical seals using a Polar coordinate system, in which micro-scale solutions were calculated and coupled into the macro-scale by use of these derivative terms. Finite difference formulations were developed to implement solutions to the problems at both scales with appropriate boundary conditions included. A demonstration of this novel scheme was carried out throughout two key problems. The first problem addressed the calculation of the derivatives of mass flux by the linearization method at the macro-scale derived from the homogenization of results at the micro-scale. The second addressed the homogenization of micro-scale solutions where periodic boundary conditions were applied to the domain to maintain the requirements of the HMM used in deriving the model.

Mesh convergence and model validation indicated that micro-scale effects were accurately captured and described at the macro-scale. Macro-scale results showed that the two-scale method agreed well with the lubrication theory in the case without topography. Micro-scale solutions showed the distribution of density ratio and resulting micro-scale cavitation occurring due to the presence of surface topography. Two parameters describing the geometry of surface topography are investigated in the present work to evaluate the influence of surface topography on the tribological performance, i.e., the amplitude and separation scale of surface topography. Variations of load-carrying capacity and friction coefficient predicted by the two-scale method were evaluated at the macro-scale by varying the amplitude of surface topography, indicating that increasing the amplitude of surface topography increased the load-carrying capacity and reduced the friction coefficient. In the current cases varying the values of separation scales shows that the decrease of separation scale leads to the decrease of load

carrying capacity. The effect of surface topography was also presented in terms of a Stribeck analysis, showing that the general shape of friction coefficient response was well reproduced compared to the established literature and that the magnitudes of friction coefficient obtained with surface topography were smaller than that without. A further study of the macro-scale surface waviness showed that any variation in the load caused by the micro-scale were smaller than the variation caused by surface waviness. This micro-scale variation cannot be obtained without the two-scale method and causes significant deviation in the tribological performance.

The presented finite-difference derivative scheme indicates a novel direction in computational engineering applications which delivers a homogenized macro-scale response including surface topography. However, further investigation should be implemented. Expanding the study to include surface deformation at both the micro- and macro-scales would allow more engineering applications to be explored. Parameterization analysis would facilitate more representative surface topographies to be investigated, and potentially carry out comparison of the influence of different topographies on the tribological performance beyond the hydrodynamic lubrication regime. Temporal terms should be considered to evaluate the two-scale model in dynamic flow problems in the future, and validation should be performed with machined textured components using experimental measurements.

Declaration of Conflicting Interests

The Authors declare that there is no conflict of interest.

Funding

The authors disclosed receipt of the following financial support for the research, authorship, and/or publication of this article: This work is supported by the Research Foundation for Advanced Talents of Jiangsu University [Grant numbers 1291110065]; and Jiangsu Provincial Government Scholarship Program.

References

1. Ruddy A, Dowson D and Taylor C. The prediction of film thickness in a mechanical face seal with circumferential waviness on both the face and the seat. *Journal of Mechanical Engineering Science*. 1982; 24: 37-43.
2. Jakobsson B and Floberg L. The finite journal bearing considering vaporization. *Transactions of Chalmers University of Technology: Gutenberg, Sweden, 1957*.
3. Olsson K-O. Cavitation in dynamically loaded bearings. *Transactions of Chalmers University of Technology*. 1965; 308.
4. Elrod HG AM. A computer program for cavitation and starvation problems. *Cavitation and related phenomena, Proceedings of the 1st Leeds-Lyon Symposium on Tribology. University of Leeds, Leeds, UK, 1974*.
5. Nyemeck AP, Brunetière N and Tournerie B. A Multiscale Approach to the Mixed Lubrication Regime: Application to Mechanical Seals. *Tribology Letters*. 2012; 47: 417-29.
6. Xiong S and Wang QJ. Steady-state hydrodynamic lubrication modeled with the Payvar-Salant mass conservation model. *Journal of Tribology*. 2012; 134: 031703.
7. Payvar P and Salant R. A computational method for cavitation in a wavy mechanical seal. *Journal of Tribology*. 1992; 114: 199-204.

8. Minet C, Brunetiere N and Tournier B. A Deterministic Mixed Lubrication Model for Mechanical Seals. *Journal Of Tribology-Transactions Of the Asme*. 2011; 133: 11.
9. Etsion I and Burstein L. A model for mechanical seals with regular microsurface structure. *Tribology Transactions*. 1996; 39: 677-83.
10. Hamilton DB, Walowit JA and Allen CM. A Theory of Lubrication by Micro Irregular. *Journal Of Basic Engineering*. 1966; 88: 177-85.
11. Gropper D, Wang L and Harvey TJ. Hydrodynamic lubrication of textured surfaces: A review of modeling techniques and key findings. *Tribology International*. 2016; 94: 509-29.
12. Patir N and Cheng HS. An Average Flow Model for Determining Effects of Three-Dimensional Roughness on Partial Hydrodynamic Lubrication. *Journal of Lubrication Technology*. 1978; 100: 12-7.
13. Patir N and Cheng HS. Application of Average Flow Model to Lubrication Between Rough Sliding Surfaces. *Journal of Lubrication Technology*. 1979; 101: 220-9.
14. König F, Rosenkranz A, Grützmacher PG, Mücklich F and Jacobs G. Effect of single- and multi-scale surface patterns on the frictional performance of journal bearings – A numerical study. *Tribology International*. 2020; 143: 106041.
15. Harp SR and Salant RF. An average flow model of rough surface lubrication with inter-asperity cavitation. *Journal Of Tribology-Transactions Of the Asme*. 2001; 123: 134-43.
16. Qiu Y and Khonsari MM. Performance Analysis of Full-Film Textured Surfaces With Consideration of Roughness Effects. *Journal Of Tribology-Transactions Of the Asme*. 2011; 133: 10.
17. Bayada G, Martin S and Vazquez C. An average flow model of the Reynolds roughness including a mass-flow preserving cavitation model. *Journal Of Tribology-Transactions Of the Asme*. 2005; 127: 793-802.
18. Almqvist A and Dasht J. The homogenization process of the Reynolds equation describing compressible liquid flow. *Tribology International*. 2006; 39: 994-1002.
19. Checo HM, Dureisseix D, Fillot N and Raisin J. A homogenized micro-elastohydrodynamic lubrication model: Accounting for non-negligible microscopic quantities. *Tribology International*. 2019; 135: 344-54.
20. Sahlin F, Almqvist A, Larsson R and Glavatskih S. Rough surface flow factors in full film lubrication based on a homogenization technique. *Tribology International*. 2007; 40: 1025-34.
21. Bayada G, Martin S and Vázquez C. Micro-roughness effects in (elasto)hydrodynamic lubrication including a mass-flow preserving cavitation model. *Tribology International*. 2006; 39: 1707-18.
22. Gao L and Hewson R. A multiscale framework for EHL and micro-EHL. *Tribology Transactions*. 2012; 55: 713-22.
23. de Boer GN, Hewson RW, Thompson HM, Gao L and Toropov VV. Two-scale EHL: Three-dimensional topography in tilted-pad bearings. *Tribology International*. 2014; 79: 111-25.
24. de Boer G, Gao L, Hewson R, Thompson H, Raske N and Toropov V. A multiscale method for optimising surface topography in elastohydrodynamic lubrication (EHL) using metamodels. *Structural and Multidisciplinary Optimization*. 2016; 54: 483-97.
25. de Boer GN, Gao L, Hewson RW and Thompson HM. Heterogeneous Multiscale Methods for modelling surface topography in Elastohydrodynamic Lubrication line contacts. *Tribology International*. 2017; 113: 262-78.
26. de Boer G and Almqvist A. On the Two-Scale Modelling of Elastohydrodynamic Lubrication in Tilted-Pad Bearings. *Lubricants*. 2018; 6: 78.
27. Elrod HG. A Cavitation Algorithm. *Journal of Lubrication Technology*. 1981; 103: 350-4.

Appendix A: Nomenclature

Symbol (dimensional)	Symbol (non-dimensional)	Description
A	\bar{A}	macro-scale surface waviness
A_t	\bar{A}_t	micro-scale topography amplitude
c		deformation – film thickness scale factor
e		percentage error
E		Young's modulus
$F_{R,\Psi_{1,2}}$	$\bar{F}_{\bar{R},\bar{\Psi}_{1,2}}$	macro-scale friction force in the radial or angular direction (upper/lower surface)
g	\bar{g}	switch function at the micro-scale
G	\bar{G}	switch function at the macro-scale
G^*	\bar{G}^*	homogenized switch function at the macro-scale
h	\bar{h}	film thickness at the micro-scale
h_t	\bar{h}_t	surface topography
H	\bar{H}	film thickness at the macro-scale
H_0	\bar{H}_0	minimum film thickness at the macro-scale
H_{00}		scaling film thickness parameter
k		material column stiffness
l_r	$l_{\bar{r}}$	length of subdomain in the radial direction
l_{ψ}	$l_{\bar{\psi}}$	length of subdomain in the angular direction
L	\bar{L}	load carrying capacity
M		longitudinal modulus
n_w		number of surface waviness on the seal face
P	\bar{P}	fluid pressure at the macro-scale
P_0	\bar{P}_0	inlet pressure
P_1	\bar{P}_1	outlet pressure
P_c	\bar{P}_c	cavitation pressure
P^*	\bar{P}^*	homogenized pressure (load per unit)
q_r	$\bar{q}_{\bar{r}}$	radial mass flux at the micro-scale
q_{ψ}	$\bar{q}_{\bar{\psi}}$	angular mass flux at the micro-scale
Q_R	\bar{Q}_R	mass flux in the radial direction
Q_{Ψ}	\bar{Q}_{Ψ}	mass flux in the angular direction
r	\bar{r}	radial coordinate in the micro-scale polar system
R	\bar{R}	radial coordinate in the polar system
R_0	\bar{R}_0	outer radius
R_1	\bar{R}_1	inner radius
S		modified Sommerfeld number
t		thickness steel surfaces
$T_{R,\Psi_{1,2}}$	$\bar{T}_{\bar{R},\bar{\Psi}_{1,2}}$	macro-scale shear stress in the radial or angular direction (upper/lower surface)
β		bulk modulus
γ		linearization factor

δ		micro-scale asperity deformation
$\Delta_{\theta,r}$	$\Delta_{\bar{\theta},\bar{r}}$	radial gradient of density ratio over the whole subdomain
$\Delta_{\theta,\psi}$	$\Delta_{\bar{\theta},\bar{\psi}}$	angular gradient of density ratio over the whole subdomain
ϵ		scale separation
η		lubricant viscosity
θ	$\bar{\theta}$	density ratio at the micro-scale
Θ	$\bar{\Theta}$	density ratio at the macro-scale
Θ^*	$\bar{\Theta}^*$	homogenized density ratio
λ		non-dimensional parameter
$\mu_{R,\Psi_{1,2}}$		friction coefficient in the radial or angular direction (upper/lower surface)
ν		Poisson's ratio
ρ_0		fluid density at cavitation pressure
ρ		fluid density
$\tau_{R,\Psi_{1,2}}$	$\bar{\tau}_{\bar{R},\bar{\Psi}_{1,2}}$	micro-scale shear stress in the radial or angular direction (upper/lower surface)
φ		relaxation factor (micro-scale)
Φ		relaxation factor (macro-scale)
ψ	$\bar{\psi}$	angular coordinate in the micro-scale polar system
Ψ	$\bar{\Psi}$	angular coordinate in the polar system
ω		angular velocity
Ω_{macro}		macro-scale computational domain
Ω_{micro}		micro-scale computational domain

Appendix B: Mass flux derivatives assuming single-scale lubrication

To solve equation (13), the derivatives of mass fluxes at the macro-scale need to be defined. Two cases are considered, i.e., with and without topography. For the case without topography, derivatives are directly derived from the Reynolds equation (equation (8)). For the case including surface topography, derivatives are represented using the linearization method where mass fluxes are obtained from micro-scale. Assuming the lubricated surface is without topography, a single-scale model is employed to predict fluid behavior in the mechanical seal. The non-dimensional mass fluxes at the macro-scale are defined as (B1) and (B2),

$$\bar{Q}_{\bar{R}} = -\lambda \bar{G} \bar{H}^3 \frac{\partial \bar{\theta}}{\partial \bar{R}} \quad (\text{B1})$$

$$\bar{Q}_{\bar{\Psi}} = \lambda \left(-\bar{G} \frac{\bar{H}^3}{\bar{R}} \frac{\partial \bar{\theta}}{\partial \bar{\Psi}} + \bar{\theta} \bar{H} \bar{R} \right) \quad (\text{B2})$$

following this the derivatives of mass fluxes with respect to $\bar{\theta}$, $\partial \bar{\theta} / \partial \bar{R}$, $\partial \bar{\theta} / \partial \bar{\Psi}$, \bar{H} are derived as (B3), (B4), (B5), (B6), (B7) and (B8),

$$\frac{\partial (\bar{R} \bar{Q}_{\bar{R}})}{\partial \bar{\theta}} = \frac{\partial (\bar{R} \bar{Q}_{\bar{R}})}{\partial \left(\frac{\partial \bar{\theta}}{\partial \bar{\Psi}} \right)} = \frac{\partial \bar{Q}_{\bar{\Psi}}}{\partial \left(\frac{\partial \bar{\theta}}{\partial \bar{R}} \right)} = 0 \quad (\text{B3})$$

$$\frac{\partial(\overline{RQ_R})}{\partial\left(\frac{\partial\overline{\Theta}}{\partial\overline{R}}\right)} = -\lambda\overline{GRH^3} \quad (B4)$$

$$\frac{\partial(\overline{RQ_R})}{\partial\overline{H}} = -3\lambda\overline{GRH^2} \frac{\partial\overline{\Theta}}{\partial\overline{R}} \quad (B5)$$

$$\frac{\partial\overline{Q_\Psi}}{\partial\overline{\Theta}} = \lambda\overline{HR} \quad (B6)$$

$$\frac{\partial\overline{Q_\Psi}}{\partial\left(\frac{\partial\overline{\Theta}}{\partial\overline{\Psi}}\right)} = -\lambda\overline{G} \frac{\overline{H^3}}{\overline{R}} \quad (B7)$$

$$\frac{\partial\overline{Q_\Psi}}{\partial\overline{H}} = \lambda \left(-3\overline{G} \frac{\overline{H^2}}{\overline{R}} \frac{\partial\overline{\Theta}}{\partial\overline{\Psi}} + \overline{\Theta R} \right) \quad (B8)$$

substitution of these expressions into equation (13) results in equation (8) which is the single-scale form of the Elrod model. These are also used as the initial solutions to the micro-scale derivatives required when carrying out the two-scale solution procedure.

Appendix C: Finite difference discretization of the macro-scale model

To improve the solver stability at the macro-scale, equation (75) was rewritten as equation (C1), which is suitable for an iterative solution based on the Gauss-Seidel method.

$$\begin{aligned} A_1 \overline{\Theta}_{i+1,j+1} - A_2 \overline{\Theta}_{i+1,j-1} - A_3 \overline{\Theta}_{i-1,j+1} + A_4 \overline{\Theta}_{i-1,j-1} + A_5 \overline{\Theta}_{i+1,j} + A_6 \overline{\Theta}_{i-1,j} + A_7 \overline{\Theta}_{i,j+1} \\ + A_8 \overline{\Theta}_{i,j-1} - A_9 \overline{\Theta}_{i,j} = B \end{aligned} \quad (C1)$$

$$i = 2, \dots, M-1 \quad j = 2, \dots, N-1$$

where $A_1 - A_9$ and B indicate the values from the previous time step which are given by equations (C2), (C3), (C4), (C5), (C6), (C7), (C8), (C9), (C10), and (C11).

$$A_1 = \frac{1}{4\Delta_{\overline{R}}\Delta_{\overline{\Psi}}} \left(\left. \frac{\partial(\overline{RQ_R})}{\partial\left(\frac{\partial\overline{\Theta}}{\partial\overline{\Psi}}\right)} \right|_{i,j}^t + \left. \frac{\partial\overline{Q_\Psi}}{\partial\left(\frac{\partial\overline{\Theta}}{\partial\overline{R}}\right)} \right|_{i,j}^t \right) \quad (C2)$$

$$A_2 = \frac{1}{4\Delta_{\overline{R}}\Delta_{\overline{\Psi}}} \left(\left. \frac{\partial(\overline{RQ_R})}{\partial\left(\frac{\partial\overline{\Theta}}{\partial\overline{\Psi}}\right)} \right|_{i,j}^t + \left. \frac{\partial\overline{Q_\Psi}}{\partial\left(\frac{\partial\overline{\Theta}}{\partial\overline{R}}\right)} \right|_{i,j}^t \right) \quad (C3)$$

$$A_3 = \frac{1}{4\Delta_{\overline{R}}\Delta_{\overline{\Psi}}} \left(\left. \frac{\partial(\overline{RQ_R})}{\partial\left(\frac{\partial\overline{\Theta}}{\partial\overline{\Psi}}\right)} \right|_{i,j}^t + \left. \frac{\partial\overline{Q_\Psi}}{\partial\left(\frac{\partial\overline{\Theta}}{\partial\overline{R}}\right)} \right|_{i,j}^t \right) \quad (C4)$$

$$A_4 = \frac{1}{4\Delta_{\bar{R}}\Delta_{\bar{\Psi}}} \left(\frac{\partial(\overline{RQ_{\bar{R}}})}{\partial\left(\frac{\partial\Theta}{\partial\Psi}\right)} \Bigg|_{i,j}^t + \frac{\partial\overline{Q_{\bar{\Psi}}}}{\partial\left(\frac{\partial\Theta}{\partial\bar{R}}\right)} \Bigg|_{i,j}^t \right) \quad (C5)$$

$$A_5 = \frac{1}{2\Delta_{\bar{R}}} \frac{\partial(\overline{RQ_{\bar{R}}})}{\partial\Theta} \Bigg|_{i,j}^t + \frac{1}{\Delta_{\bar{R}}^2} \frac{\partial(\overline{RQ_{\bar{R}}})}{\partial\left(\frac{\partial\Theta}{\partial\bar{R}}\right)} \Bigg|_{i,j}^t \quad (C6)$$

$$A_6 = -\frac{1}{2\Delta_{\bar{R}}} \frac{\partial(\overline{RQ_{\bar{R}}})}{\partial\Theta} \Bigg|_{i,j}^t + \frac{1}{\Delta_{\bar{R}}^2} \frac{\partial(\overline{RQ_{\bar{R}}})}{\partial\left(\frac{\partial\Theta}{\partial\bar{R}}\right)} \Bigg|_{i,j}^t \quad (C7)$$

$$A_7 = \frac{1}{2\Delta_{\bar{\Psi}}} \frac{\partial\overline{Q_{\bar{\Psi}}}}{\partial\Theta} \Bigg|_{i,j}^t + \frac{1}{\Delta_{\bar{\Psi}}^2} \frac{\partial\overline{Q_{\bar{\Psi}}}}{\partial\left(\frac{\partial\Theta}{\partial\Psi}\right)} \Bigg|_{i,j}^t \quad (C8)$$

$$A_8 = -\frac{1}{2\Delta_{\bar{\Psi}}} \frac{\partial\overline{Q_{\bar{\Psi}}}}{\partial\Theta} \Bigg|_{i,j}^t + \frac{1}{\Delta_{\bar{\Psi}}^2} \frac{\partial\overline{Q_{\bar{\Psi}}}}{\partial\left(\frac{\partial\Theta}{\partial\Psi}\right)} \Bigg|_{i,j}^t \quad (C9)$$

$$A_9 = 2 \left(\frac{1}{\Delta_{\bar{R}}^2} \frac{\partial(\overline{RQ_{\bar{R}}})}{\partial\left(\frac{\partial\Theta}{\partial\bar{R}}\right)} \Bigg|_{i,j}^t + \frac{1}{\Delta_{\bar{\Psi}}^2} \frac{\partial\overline{Q_{\bar{\Psi}}}}{\partial\left(\frac{\partial\Theta}{\partial\Psi}\right)} \Bigg|_{i,j}^t \right) \quad (C10)$$

$$\begin{aligned}
B = & \left(\frac{\partial(\overline{RQ}_{\overline{R}})}{\partial \overline{H}} \Big|_{i,j}^{t-1} - \frac{\partial(\overline{RQ}_{\overline{R}})}{\partial \overline{H}} \Big|_{i,j}^t \right) \cdot \frac{\overline{H}_{i+1,j} - \overline{H}_{i-1,j}}{2\Delta_{\overline{R}}} + \left(\frac{\partial \overline{Q}_{\overline{\Psi}}}{\partial \overline{H}} \Big|_{i,j}^{t-1} - \frac{\partial \overline{Q}_{\overline{\Psi}}}{\partial \overline{H}} \Big|_{i,j}^t \right) \cdot \frac{\overline{H}_{i,j+1} - \overline{H}_{i,j-1}}{2\Delta_{\overline{\Psi}}} \quad (C11) \\
& + \frac{\partial(\overline{RQ}_{\overline{R}})}{\partial \overline{\Theta}} \Big|_{i,j}^{t-1} \cdot \frac{\overline{\Theta}_{i+1,j}^{t-1} - \overline{\Theta}_{i-1,j}^{t-1}}{2\Delta_{\overline{R}}} + \frac{\partial \overline{Q}_{\overline{\Psi}}}{\partial \overline{\Theta}} \Big|_{i,j}^{t-1} \cdot \frac{\overline{\Theta}_{i,j+1}^{t-1} - \overline{\Theta}_{i,j-1}^{t-1}}{2\Delta_{\overline{\Psi}}} \\
& + \frac{\partial(\overline{RQ}_{\overline{R}})}{\partial \left(\frac{\partial \overline{\Theta}}{\partial \overline{R}} \right)} \Big|_{i,j}^{t-1} \cdot \frac{\overline{\Theta}_{i+1,j}^{t-1} - 2\overline{\Theta}_{i,j}^{t-1} + \overline{\Theta}_{i-1,j}^{t-1}}{\Delta_{\overline{R}}^2} + \frac{\partial \overline{Q}_{\overline{\Psi}}}{\partial \left(\frac{\partial \overline{\Theta}}{\partial \overline{\Psi}} \right)} \Big|_{i,j}^{t-1} \\
& \cdot \frac{\overline{\Theta}_{i,j+1}^{t-1} - 2\overline{\Theta}_{i,j}^{t-1} + \overline{\Theta}_{i,j-1}^{t-1}}{\Delta_{\overline{\Psi}}^2} + \left(\frac{\partial(\overline{RQ}_{\overline{R}})}{\partial \left(\frac{\partial \overline{\Theta}}{\partial \overline{\Psi}} \right)} \Big|_{i,j}^{t-1} + \frac{\partial \overline{Q}_{\overline{\Psi}}}{\partial \left(\frac{\partial \overline{\Theta}}{\partial \overline{R}} \right)} \Big|_{i,j}^{t-1} \right) \\
& \cdot \frac{\overline{\Theta}_{i+1,j+1}^{t-1} - \overline{\Theta}_{i+1,j-1}^{t-1} - \overline{\Theta}_{i-1,j+1}^{t-1} + \overline{\Theta}_{i-1,j-1}^{t-1}}{4\Delta_{\overline{R}}\Delta_{\overline{\Psi}}}
\end{aligned}$$

Equation (C1) was treated as systems of linear equations with boundary conditions defined using equations (16) (17) (18), and (30). The discretization of these was equations (C12), (C13), (C14) and (C15).

$$\overline{\Theta}_{i,j} = \overline{P}_0 - \overline{P}_c + \frac{1}{\lambda} \quad (C12)$$

$$i = M \quad j = 1, \dots, N$$

$$\overline{\Theta}_{i,j} = \overline{P}_1 - \overline{P}_c + \frac{1}{\lambda} \quad (C13)$$

$$i = 1 \quad j = 1, \dots, N$$

$$\overline{\Theta}_{i,j} - \overline{\Theta}_{i,N} = 0 \quad (C14)$$

$$i = 2, \dots, M-1 \quad j = 1$$

$$\overline{\Theta}_{i,j} - \overline{\Theta}_{i,j-1} + \overline{\Theta}_{i,1} - \overline{\Theta}_{i,2} = 0 \quad (C15)$$

$$i = 2, \dots, M-1 \quad j = N$$

In the case of including surface topography, derivatives of mass fluxes at the macro-scale, which need to be obtained for solving equation (C1) using the linearization method described in Section 2.2.3, were equations (C16), (C17), (C18), (C19), (C20), (C21), (C22) and (C23),

$$\frac{\partial \bar{Q}_{\bar{\Psi}}}{\partial \left(\frac{\partial \bar{\Theta}}{\partial \bar{\Psi}} \right)} \Bigg|_{i,j}^t = \frac{1}{2\Delta_{\frac{\partial \bar{\Theta}}{\partial \bar{\Psi}}}} \left(\bar{Q}_{\bar{\Psi}} \left(\frac{\partial \bar{\Theta}}{\partial \bar{R}} \Bigg|_{i,j}^t, \frac{\partial \bar{\Theta}}{\partial \bar{\Psi}} \Bigg|_{i,j}^t + \Delta_{\frac{\partial \bar{\Theta}}{\partial \bar{\Psi}}}, \bar{H}_{i,j}, \bar{R}_{i,j}, \bar{\Psi}_{i,j} \right) \right. \tag{C22}$$

$$\left. - \bar{Q}_{\bar{\Psi}} \left(\frac{\partial \bar{\Theta}}{\partial \bar{R}} \Bigg|_{i,j}^t, \frac{\partial \bar{\Theta}}{\partial \bar{\Psi}} \Bigg|_{i,j}^t - \Delta_{\frac{\partial \bar{\Theta}}{\partial \bar{\Psi}}}, \bar{H}_{i,j}, \bar{R}_{i,j}, \bar{\Psi}_{i,j} \right) \right)$$

$$\frac{\partial \bar{Q}_{\bar{\Psi}}}{\partial \bar{H}} \Bigg|_{i,j}^t = \frac{1}{2\Delta_{\bar{H}}} \left(\bar{Q}_{\bar{\Psi}} \left(\frac{\partial \bar{\Theta}}{\partial \bar{R}} \Bigg|_{i,j}^t, \frac{\partial \bar{\Theta}}{\partial \bar{\Psi}} \Bigg|_{i,j}^t, \bar{H}_{i,j} + \Delta_{\bar{H}}, \bar{R}_{i,j}, \bar{\Psi}_{i,j} \right) \right. \tag{C23}$$

$$\left. - \bar{Q}_{\bar{\Psi}} \left(\frac{\partial \bar{\Theta}}{\partial \bar{R}} \Bigg|_{i,j}^t, \frac{\partial \bar{\Theta}}{\partial \bar{\Psi}} \Bigg|_{i,j}^t, \bar{H}_{i,j} - \Delta_{\bar{H}}, \bar{R}_{i,j}, \bar{\Psi}_{i,j} \right) \right)$$

here, micro-scale results required at each i, j for every iteration time are functions of variables $\bar{\Theta}, \partial \bar{\Theta} / \partial \bar{R}, \partial \bar{\Theta} / \partial \bar{\Psi}, \bar{H}, \bar{R}, \bar{\Psi}$ from the macro-scale, which are homogenized equations (66) –(68).

Each term used to calculate the derivatives are listed here in equations (C24), (C25), (C26), (C27), (C28), (C29), (C30) and (C31),

$$\bar{Q}_{\bar{R}, \bar{\Psi}} \left(\frac{\partial \bar{\Theta}}{\partial \bar{R}} \Bigg|_{i,j}^t + \Delta_{\bar{\Theta}}, \frac{\partial \bar{\Theta}}{\partial \bar{R}} \Bigg|_{i,j}^t, \frac{\partial \bar{\Theta}}{\partial \bar{\Psi}} \Bigg|_{i,j}^t, \bar{H}_{i,j}, \bar{R}_{i,j}, \bar{\Psi}_{i,j} \right) \tag{C24}$$

$$\bar{Q}_{\bar{R}, \bar{\Psi}} \left(\frac{\partial \bar{\Theta}}{\partial \bar{R}} \Bigg|_{i,j}^t - \Delta_{\bar{\Theta}}, \frac{\partial \bar{\Theta}}{\partial \bar{R}} \Bigg|_{i,j}^t, \frac{\partial \bar{\Theta}}{\partial \bar{\Psi}} \Bigg|_{i,j}^t, \bar{H}_{i,j}, \bar{R}_{i,j}, \bar{\Psi}_{i,j} \right) \tag{C25}$$

$$\bar{Q}_{\bar{R}, \bar{\Psi}} \left(\frac{\partial \bar{\Theta}}{\partial \bar{R}} \Bigg|_{i,j}^t + \Delta_{\frac{\partial \bar{\Theta}}{\partial \bar{R}}}, \frac{\partial \bar{\Theta}}{\partial \bar{R}} \Bigg|_{i,j}^t, \frac{\partial \bar{\Theta}}{\partial \bar{\Psi}} \Bigg|_{i,j}^t, \bar{H}_{i,j}, \bar{R}_{i,j}, \bar{\Psi}_{i,j} \right) \tag{C26}$$

$$\bar{Q}_{\bar{R}, \bar{\Psi}} \left(\frac{\partial \bar{\Theta}}{\partial \bar{R}} \Bigg|_{i,j}^t - \Delta_{\frac{\partial \bar{\Theta}}{\partial \bar{R}}}, \frac{\partial \bar{\Theta}}{\partial \bar{R}} \Bigg|_{i,j}^t, \frac{\partial \bar{\Theta}}{\partial \bar{\Psi}} \Bigg|_{i,j}^t, \bar{H}_{i,j}, \bar{R}_{i,j}, \bar{\Psi}_{i,j} \right) \tag{C27}$$

$$\bar{Q}_{\bar{R}, \bar{\Psi}} \left(\frac{\partial \bar{\Theta}}{\partial \bar{R}} \Bigg|_{i,j}^t, \frac{\partial \bar{\Theta}}{\partial \bar{\Psi}} \Bigg|_{i,j}^t + \Delta_{\frac{\partial \bar{\Theta}}{\partial \bar{\Psi}}}, \bar{H}_{i,j}, \bar{R}_{i,j}, \bar{\Psi}_{i,j} \right) \tag{C28}$$

$$\bar{Q}_{\bar{R}, \bar{\Psi}} \left(\frac{\partial \bar{\Theta}}{\partial \bar{R}} \Bigg|_{i,j}^t, \frac{\partial \bar{\Theta}}{\partial \bar{\Psi}} \Bigg|_{i,j}^t - \Delta_{\frac{\partial \bar{\Theta}}{\partial \bar{\Psi}}}, \bar{H}_{i,j}, \bar{R}_{i,j}, \bar{\Psi}_{i,j} \right) \tag{C29}$$

$$\bar{Q}_{\bar{R}, \bar{\Psi}} \left(\frac{\partial \bar{\Theta}}{\partial \bar{R}} \Bigg|_{i,j}^t, \frac{\partial \bar{\Theta}}{\partial \bar{\Psi}} \Bigg|_{i,j}^t, \bar{H}_{i,j} + \Delta_{\bar{H}}, \bar{R}_{i,j}, \bar{\Psi}_{i,j} \right) \tag{C30}$$

$$\bar{Q}_{\bar{R}, \bar{\Psi}} \left(\frac{\partial \bar{\Theta}}{\partial \bar{R}} \Bigg|_{i,j}^t, \frac{\partial \bar{\Theta}}{\partial \bar{\Psi}} \Bigg|_{i,j}^t, \bar{H}_{i,j} - \Delta_{\bar{H}}, \bar{R}_{i,j}, \bar{\Psi}_{i,j} \right) \tag{C31}$$

where the variables $\Delta_{\bar{\Theta}}, \Delta_{\frac{\partial \bar{\Theta}}{\partial \bar{R}}}, \Delta_{\frac{\partial \bar{\Theta}}{\partial \bar{\Psi}}}, \Delta_{\bar{H}}$ were obtained according to equation (72).

After the convergence of macro-scale solution was achieved with the iteration number t , micro-scale results at each macro-scale node were obtained, defining the mass flux (equation (C32)), homogenized density ratio (equation (C33)), shear stress (equation (C34)) at each macro-scale node,

$$\bar{Q}_{\bar{R}, \bar{\Psi}} \left(\left. \frac{\partial \bar{\Theta}}{\partial \bar{R}} \right|_{i,j}^t, \left. \frac{\partial \bar{\Theta}}{\partial \bar{\Psi}} \right|_{i,j}^t, \bar{H}_{i,j}, \bar{R}_{i,j}, \bar{\Psi}_{i,j} \right) \quad (C32)$$

$$\bar{\Theta} \left(\left. \frac{\partial \bar{\Theta}}{\partial \bar{R}} \right|_{i,j}^t, \left. \frac{\partial \bar{\Theta}}{\partial \bar{\Psi}} \right|_{i,j}^t, \bar{H}_{i,j}, \bar{R}_{i,j}, \bar{\Psi}_{i,j} \right) \quad (C33)$$

$$\bar{T}_{\bar{R}, \bar{\Psi}, 1,2} \left(\left. \frac{\partial \bar{\Theta}}{\partial \bar{R}} \right|_{i,j}^t, \left. \frac{\partial \bar{\Theta}}{\partial \bar{\Psi}} \right|_{i,j}^t, \bar{H}_{i,j}, \bar{R}_{i,j}, \bar{\Psi}_{i,j} \right) \quad (C34)$$

gradients and integral quantities are also obtained by finite differencing at the macro-scale.

At each solution time in the macro-scale model, the values of the gradients of $\bar{\Theta}$ at each location are updated with the current solutions to $\bar{\Theta}$, corresponding gradients, and the previous known $\bar{\Theta}$ values. The following equations describe the finite difference form of these gradients at each solution time across the entire macro-scale domain (C35), (C36), (C37), (C38) and (C39).

$$\left. \frac{\partial \bar{\Theta}}{\partial \bar{R}} \right|_{i,j}^t = \Phi \left. \frac{\partial \bar{\Theta}}{\partial \bar{R}} \right|_{i,j}^{t-1} + (1 - \Phi) \frac{\bar{\Theta}_{i+1,j} - \bar{\Theta}_{i-1,j}}{2\Delta_{\bar{R}}} \quad (C35)$$

$$\left. \frac{\partial \bar{\Theta}}{\partial \bar{\Psi}} \right|_{i,j}^t = \Phi \left. \frac{\partial \bar{\Theta}}{\partial \bar{\Psi}} \right|_{i,j}^{t-1} + (1 - \Phi) \frac{\bar{\Theta}_{i,j+1} - \bar{\Theta}_{i,j-1}}{2\Delta_{\bar{\Psi}}} \quad (C36)$$

$i = 2, \dots, M - 1 \quad j = 2, \dots, N - 1$

$$\left. \frac{\partial \bar{\Theta}}{\partial \bar{R}} \right|_{i,j}^t = \Phi \left. \frac{\partial \bar{\Theta}}{\partial \bar{R}} \right|_{i,j}^{t-1} + (1 - \Phi) \frac{\bar{\Theta}_{i+1,j} - \bar{\Theta}_{i,j}}{\Delta_{\bar{R}}} \quad (C36)$$

$$\left. \frac{\partial \bar{\Theta}}{\partial \bar{\Psi}} \right|_{i,j}^t = \Phi \left. \frac{\partial \bar{\Theta}}{\partial \bar{\Psi}} \right|_{i,j}^{t-1} + (1 - \Phi) \frac{\bar{\Theta}_{i,j+1} - \bar{\Theta}_{i,j-1}}{2\Delta_{\bar{\Psi}}} \quad (C37)$$

$i = 1 \quad j = 2, \dots, N - 1$

$$\left. \frac{\partial \bar{\Theta}}{\partial \bar{R}} \right|_{i,j}^t = \Phi \left. \frac{\partial \bar{\Theta}}{\partial \bar{R}} \right|_{i,j}^{t-1} + (1 - \Phi) \frac{\bar{\Theta}_{i,j} - \bar{\Theta}_{i-1,j}}{\Delta_{\bar{R}}} \quad (C37)$$

$$\left. \frac{\partial \bar{\Theta}}{\partial \bar{\Psi}} \right|_{i,j}^t = \Phi \left. \frac{\partial \bar{\Theta}}{\partial \bar{\Psi}} \right|_{i,j}^{t-1} + (1 - \Phi) \frac{\bar{\Theta}_{i,j+1} - \bar{\Theta}_{i,j-1}}{2\Delta_{\bar{\Psi}}} \quad (C38)$$

$i = M \quad j = 2, \dots, N - 1$

$$\left. \frac{\partial \bar{\Theta}}{\partial \bar{R}} \right|_{i,j}^t = \Phi \left. \frac{\partial \bar{\Theta}}{\partial \bar{R}} \right|_{i,j}^{t-1} + (1 - \Phi) \frac{\bar{\Theta}_{i+1,j} - \bar{\Theta}_{i-1,j}}{2\Delta_{\bar{R}}} \quad (C38)$$

$$\begin{aligned}
\left. \frac{\partial \bar{\Theta}}{\partial \bar{\Psi}} \right|_{i,j}^t &= \Phi \left. \frac{\partial \bar{\Theta}}{\partial \bar{\Psi}} \right|_{i,j}^{t-1} + (1 - \Phi) \frac{\bar{\Theta}_{i,j+1} - \bar{\Theta}_{i,j}}{\Delta \bar{\Psi}} \\
i &= 2, \dots, M-1 \quad j = 1 \\
\left. \frac{\partial \bar{\Theta}}{\partial \bar{R}} \right|_{i,j}^t &= \Phi \left. \frac{\partial \bar{\Theta}}{\partial \bar{R}} \right|_{i,j}^{t-1} + (1 - \Phi) \frac{\bar{\Theta}_{i+1,j} - \bar{\Theta}_{i-1,j}}{2\Delta \bar{R}} \\
\left. \frac{\partial \bar{\Theta}}{\partial \bar{\Psi}} \right|_{i,j}^t &= \Phi \left. \frac{\partial \bar{\Theta}}{\partial \bar{\Psi}} \right|_{i,j}^{t-1} + (1 - \Phi) \frac{\bar{\Theta}_{i,j} - \bar{\Theta}_{i,j-1}}{\Delta \bar{\Psi}} \\
i &= 2, \dots, M-1 \quad j = N
\end{aligned} \tag{C39}$$

The non-dimensional load-carrying capacity and friction forces are derived using the trapezoid rule to numerically discretize equations (31) and (37), resulting in (C40) and (C41),

$$\bar{L} = \frac{\Delta \bar{R} \Delta \bar{\Psi}}{8} \sum_{i=1}^{M-1} \sum_{j=1}^{N-1} (\bar{R}_{i,j} + \bar{R}_{i+1,j}) (\bar{P}_{i,j}^* + \bar{P}_{i+1,j}^* + \bar{P}_{i,j+1}^* + \bar{P}_{i+1,j+1}^*) \tag{C40}$$

$$\begin{aligned}
\bar{F}_{\bar{R}, \bar{\Psi}}_{1,2} &= \frac{\Delta \bar{R} \Delta \bar{\Psi}}{8} \sum_{i=1}^{M-1} \sum_{j=1}^{N-1} (\bar{R}_{i,j} + \bar{R}_{i+1,j}) \left(\bar{T}_{\bar{R}, \bar{\Psi}}_{1,2,i,j} + \bar{T}_{\bar{R}, \bar{\Psi}}_{1,2,i+1,j} + \bar{T}_{\bar{R}, \bar{\Psi}}_{1,2,i,j+1} \right. \\
&\quad \left. + \bar{T}_{\bar{R}, \bar{\Psi}}_{1,2,i+1,j+1} \right) \tag{C41}
\end{aligned}$$

where the nodal values of the load per unit area $\bar{P}_{i,j}^*$ are obtained in relation to the homogenized switch function $\bar{G}_{i,j}^*$ and homogenized density ratio $\bar{\Theta}_{i,j}^*$. The discrete forms of these relations are given by (C42) and (C43).

$$\bar{G}_{i,j}^* = \begin{cases} \frac{1}{\lambda} & \bar{\Theta}_{i,j}^* > \frac{1}{\lambda} \\ 0 & \bar{\Theta}_{i,j}^* \leq \frac{1}{\lambda} \end{cases} \tag{C42}$$

$$\begin{aligned}
i &= 1, \dots, M \quad j = 1, \dots, N \\
\bar{P}_{i,j}^* &= \bar{P}_c + \bar{G}_{i,j}^* \left(\bar{\Theta}_{i,j}^* - \frac{1}{\lambda} \right) \tag{C43} \\
i &= 1, \dots, M \quad j = 1, \dots, N
\end{aligned}$$

Appendix D: Finite difference discretization of the micro-scale model

At the micro-scale and in satisfying $\bar{g}_{i,j}^t = \frac{1}{\lambda}$, equation (80) was converted into equation (D1),

$$\begin{aligned}
& \overline{\theta}_{i+1,j} \left(\frac{\bar{r}_{i+1/2,j} \bar{h}_{i+1/2,j}^{-3}}{\Delta_{\bar{r}}^2} \right) + \overline{\theta}_{i-1,j} \left(\frac{\bar{r}_{i-1/2,j} \bar{h}_{i-1/2,j}^{-3}}{\Delta_{\bar{r}}^2} \right) + \overline{\theta}_{ij+1} \left(\frac{\bar{h}_{ij+1/2}^{-3}}{\bar{r}_{ij} \Delta_{\bar{\psi}}^2} \right) + \overline{\theta}_{ij-1} \left(\frac{\bar{h}_{ij-1/2}^{-3}}{\bar{r}_{ij} \Delta_{\bar{\psi}}^2} \right) \quad (D1) \\
& - \overline{\theta}_{ij} \left(\frac{\bar{r}_{i+1/2,j} \bar{h}_{i+1/2,j}^{-3} + \bar{r}_{i-1/2,j} \bar{h}_{i-1/2,j}^{-3}}{\Delta_{\bar{r}}^2} + \frac{\bar{h}_{ij+1/2}^{-3} + \bar{h}_{ij-1/2}^{-3}}{\bar{r}_{ij} \Delta_{\bar{\psi}}^2} \right) \\
& = \lambda \bar{r}_{ij} \frac{\overline{\theta}_{ij+1}^{t-1} \bar{h}_{ij+1} - \overline{\theta}_{ij-1}^{t-1} \bar{h}_{ij-1}}{2\Delta_{\bar{\psi}}^-} \\
& \quad i = 2, \dots, n-1 \quad j = 2, \dots, n-1
\end{aligned}$$

To do this, equation (42) was discretized using the finite-difference method for the density ratio to obtain micro-scale mass fluxes in each coordinate direction using equations (45) and (46). In satisfying $\bar{g}_{ij}^t = \frac{1}{\lambda}$, the discretized expression was described as equation (D2),

$$\begin{aligned}
& a_1 \overline{\theta}_{i+1,j} + a_2 \overline{\theta}_{i-1,j} + a_3 \overline{\theta}_{ij+1} + a_4 \overline{\theta}_{ij-1} - a_5 \overline{\theta}_{ij} = b \quad (D2) \\
& \quad i = 2, \dots, m-1 \quad j = 2, \dots, n-1
\end{aligned}$$

in which $a_1 - a_5$ and b are known values from previous time step (D3), (D4), (D5), (D6), (D7) and (D8).

$$a_1 = \left(\frac{\bar{r}_{i+1/2,j} \bar{h}_{i+1/2,j}^{-3}}{\Delta_{\bar{r}}^2} \right) \quad (D3)$$

$$a_2 = \left(\frac{\bar{r}_{i-1/2,j} \bar{h}_{i-1/2,j}^{-3}}{\Delta_{\bar{r}}^2} \right) \quad (D4)$$

$$a_3 = \left(\frac{\bar{h}_{ij+1/2}^{-3}}{\bar{r}_{ij} \Delta_{\bar{\psi}}^2} \right) \quad (D5)$$

$$a_4 = \left(\frac{\bar{h}_{ij-1/2}^{-3}}{\bar{r}_{ij} \Delta_{\bar{\psi}}^2} \right) \quad (D6)$$

$$a_5 = \left(\frac{\bar{r}_{i+1/2,j} \bar{h}_{i+1/2,j}^{-3} + \bar{r}_{i-1/2,j} \bar{h}_{i-1/2,j}^{-3}}{\Delta_{\bar{r}}^2} + \frac{\bar{h}_{ij+1/2}^{-3} + \bar{h}_{ij-1/2}^{-3}}{\bar{r}_{ij} \Delta_{\bar{\psi}}^2} \right) \quad (D7)$$

$$b = \lambda \bar{r}_{ij} \frac{\overline{\theta}_{ij+1}^{t-1} \bar{h}_{ij+1} - \overline{\theta}_{ij-1}^{t-1} \bar{h}_{ij-1}}{2\Delta_{\bar{\psi}}^-} \quad (D8)$$

The following relations were also defined using finite difference schemes (equations (D9), (D10), (D11)).

$$\bar{r}_{i\pm 1/2,j} = \frac{\bar{r}_{i\pm 1,j} + \bar{r}_{i,j}}{2} \quad (D9)$$

$$\bar{h}_{i\pm 1/2,j} = \frac{\bar{h}_{i\pm 1,j} + \bar{h}_{i,j}}{2} \quad (D10)$$

$$\bar{h}_{i,j\pm 1/2} = \frac{\bar{h}_{i,j\pm 1} + \bar{h}_{i,j}}{2} \quad (D11)$$

In satisfying $\bar{g}_{i,j}^t = 0$, equation (80) was converted into equation (D12),

$$\bar{h}_{i,j+1} \bar{\theta}_{i,j+1} + \bar{h}_{i,j-1} \bar{\theta}_{i,j-1} - 2\bar{h}_{i,j} \bar{\theta}_{i,j} = 0 \quad (D12)$$

$$i = 2, \dots, m-1 \quad j = 2, \dots, n-1$$

and the discrete form of the node constraint at the micro-scale was equation (D13),

$$\bar{\theta}_{i,j} = \bar{\Theta} \quad (D13)$$

$$i = m/2 \quad j = n/2$$

$$\text{mod}(m, n) = 0$$

which was added to the system of equations as an additional degree of freedom. Boundary conditions and corner node constraints were rewritten in the finite difference form using equations (D14), (D15), (D16), (D17), (D18), (D19), (D20) and (D21).

$$\bar{\theta}_{i,j} - \bar{\theta}_{m,j} = -\Delta_{\bar{\theta}, \bar{r}} \quad (D14)$$

$$i = 1 \quad j = 2, \dots, n-1$$

$$\bar{\theta}_{i,j} - \bar{\theta}_{i,n} = -\Delta_{\bar{\theta}, \bar{\psi}} \quad (D15)$$

$$i = 2, \dots, m-1 \quad j = 1$$

$$-\bar{\theta}_{i,j} + \bar{\theta}_{i-1,j} - \bar{\theta}_{1,j} + \bar{\theta}_{2,j} = 0 \quad (D16)$$

$$i = m \quad j = 2, \dots, n-1$$

$$-\bar{\theta}_{i,j} + \bar{\theta}_{i,j-1} - \bar{\theta}_{i,1} + \bar{\theta}_{i,2} = 0 \quad (D17)$$

$$i = 2, \dots, m-1 \quad j = n$$

$$2\bar{\theta}_{i,j} - \bar{\theta}_{m,j} - \bar{\theta}_{i,n} = -\Delta_{\bar{\theta}, \bar{r}} - \Delta_{\bar{\theta}, \bar{\psi}} \quad (D18)$$

$$i = 1 \quad j = 1$$

$$2\bar{\theta}_{i,j} - \bar{\theta}_{1,j} - \bar{\theta}_{i,1} = \Delta_{\bar{\theta}, \bar{r}} + \Delta_{\bar{\theta}, \bar{\psi}} \quad (D19)$$

$$i = m \quad j = n$$

$$\bar{\theta}_{i,j} \left(\frac{1}{\Delta_{\bar{r}}} + \frac{1}{\Delta_{\bar{\psi}}} \right) - \bar{\theta}_{i-1,j} \frac{1}{\Delta_{\bar{r}}} - \bar{\theta}_{2,j} \frac{1}{\Delta_{\bar{r}}} + \bar{\theta}_{1,j} \frac{1}{\Delta_{\bar{r}}} - \bar{\theta}_{i,j+1} \frac{1}{\Delta_{\bar{\psi}}} + \bar{\theta}_{i,n} \frac{1}{\Delta_{\bar{\psi}}} - \bar{\theta}_{i,n-1} \frac{1}{\Delta_{\bar{\psi}}} = 0 \quad (D20)$$

$$i = m \quad j = 1$$

$$-\bar{\theta}_{i,j} \left(\frac{1}{\Delta_{\bar{r}}} + \frac{1}{\Delta_{\bar{\psi}}} \right) + \bar{\theta}_{i+1,j} \frac{1}{\Delta_{\bar{r}}} - \bar{\theta}_{m,j} \frac{1}{\Delta_{\bar{r}}} + \bar{\theta}_{m-1,j} \frac{1}{\Delta_{\bar{r}}} + \bar{\theta}_{i,j-1} \frac{1}{\Delta_{\bar{\psi}}} + \bar{\theta}_{i,2} \frac{1}{\Delta_{\bar{\psi}}} - \bar{\theta}_{i,1} \frac{1}{\Delta_{\bar{\psi}}} \quad (D21)$$

$$= 0$$

$$i = 1 \quad j = n$$

At the micro-scale, gradients of $\bar{\theta}$ are determined at each solution time according to the finite

difference scheme outlined by (D22), (D23), (D24), (D25) and (D26), which is similar in format to the gradient calculation at the macro-scale.

$$\left. \frac{\partial \bar{\theta}}{\partial \bar{r}} \right|_{i,j}^t = \varphi \left. \frac{\partial \bar{\theta}}{\partial \bar{r}} \right|_{i,j}^{t-1} + (1 - \varphi) \frac{\bar{\theta}_{i+1,j} - \bar{\theta}_{i-1,j}}{2\Delta_{\bar{r}}} \quad (\text{D22})$$

$$\left. \frac{\partial \bar{\theta}}{\partial \bar{\psi}} \right|_{i,j}^t = \varphi \left. \frac{\partial \bar{\theta}}{\partial \bar{\psi}} \right|_{i,j}^{t-1} + (1 - \varphi) \frac{\bar{\theta}_{i,j+1} - \bar{\theta}_{i,j-1}}{2\Delta_{\bar{\psi}}}$$

$$i = 2, \dots, m - 1 \quad j = 2, \dots, n - 1$$

$$\left. \frac{\partial \bar{\theta}}{\partial \bar{r}} \right|_{i,j}^t = \varphi \left. \frac{\partial \bar{\theta}}{\partial \bar{r}} \right|_{i,j}^{t-1} + (1 - \varphi) \frac{\bar{\theta}_{i+1,j} - \bar{\theta}_{i,j}}{\Delta_{\bar{r}}} \quad (\text{D23})$$

$$\left. \frac{\partial \bar{\theta}}{\partial \bar{\psi}} \right|_{i,j}^t = \varphi \left. \frac{\partial \bar{\theta}}{\partial \bar{\psi}} \right|_{i,j}^{t-1} + (1 - \varphi) \frac{\bar{\theta}_{i,j+1} - \bar{\theta}_{i,j-1}}{2\Delta_{\bar{\psi}}}$$

$$i = 1 \quad j = 2, \dots, n - 1$$

$$\left. \frac{\partial \bar{\theta}}{\partial \bar{r}} \right|_{i,j}^t = \varphi \left. \frac{\partial \bar{\theta}}{\partial \bar{r}} \right|_{i,j}^{t-1} + (1 - \varphi) \frac{\bar{\theta}_{i,j} - \bar{\theta}_{i-1,j}}{\Delta_{\bar{r}}} \quad (\text{D24})$$

$$\left. \frac{\partial \bar{\theta}}{\partial \bar{\psi}} \right|_{i,j}^t = \varphi \left. \frac{\partial \bar{\theta}}{\partial \bar{\psi}} \right|_{i,j}^{t-1} + (1 - \varphi) \frac{\bar{\theta}_{i,j+1} - \bar{\theta}_{i,j-1}}{2\Delta_{\bar{\psi}}}$$

$$i = m \quad j = 2, \dots, n - 1$$

$$\left. \frac{\partial \bar{\theta}}{\partial \bar{r}} \right|_{i,j}^t = \varphi \left. \frac{\partial \bar{\theta}}{\partial \bar{r}} \right|_{i,j}^{t-1} + (1 - \varphi) \frac{\bar{\theta}_{i+1,j} - \bar{\theta}_{i-1,j}}{2\Delta_{\bar{r}}} \quad (\text{D25})$$

$$\left. \frac{\partial \bar{\theta}}{\partial \bar{\psi}} \right|_{i,j}^t = \varphi \left. \frac{\partial \bar{\theta}}{\partial \bar{\psi}} \right|_{i,j}^{t-1} + (1 - \varphi) \frac{\bar{\theta}_{i,j+1} - \bar{\theta}_{i,j}}{\Delta_{\bar{\psi}}}$$

$$i = 2, \dots, m - 1 \quad j = 1$$

$$\left. \frac{\partial \bar{\theta}}{\partial \bar{r}} \right|_{i,j}^t = \varphi \left. \frac{\partial \bar{\theta}}{\partial \bar{r}} \right|_{i,j}^{t-1} + (1 - \varphi) \frac{\bar{\theta}_{i+1,j} - \bar{\theta}_{i-1,j}}{2\Delta_{\bar{r}}} \quad (\text{D26})$$

$$\left. \frac{\partial \bar{\theta}}{\partial \bar{\psi}} \right|_{i,j}^t = \varphi \left. \frac{\partial \bar{\theta}}{\partial \bar{\psi}} \right|_{i,j}^{t-1} + (1 - \varphi) \frac{\bar{\theta}_{i,j} - \bar{\theta}_{i,j-1}}{\Delta_{\bar{\psi}}}$$

$$i = 2, \dots, m - 1 \quad j = n$$

The homogenized mass fluxes are obtained by application of the trapezoid rule which yields (D27) and (D28),

$$\bar{Q}_{\bar{r}} = \frac{\Delta_{\bar{\psi}}}{2\Delta_{\bar{\psi}}} \sum_{j=1}^{j=n-1} (\bar{q}_{\bar{r},i,j} + \bar{q}_{\bar{r},i,j+1}) \quad (\text{D27})$$

$$i = 1, m$$

$$\bar{Q}_{\bar{\Psi}} = \frac{\Delta_{\bar{r}}}{2l_{\bar{r}}} \sum_{i=1}^{i=m-1} (\bar{q}_{\bar{\Psi}_{i,j}} + \bar{q}_{\bar{\Psi}_{i+1,j}}) \quad (D28)$$

$$j = 1, n$$

where the discrete forms of the micro-scale mass fluxes are given by (D29) and (D30).

$$\bar{q}_{\bar{r}_{i,j}} = -\lambda \bar{g}_{i,j}^t \bar{h}_{i,j}^{-3} \left. \frac{\partial \bar{\theta}}{\partial \bar{r}} \right|_{i,j}^t \quad (D29)$$

$$i = 1, \dots, m \quad j = 1, \dots, n$$

$$\bar{q}_{\bar{\Psi}_{i,j}} = \lambda \left(-\bar{g}_{i,j}^t \frac{\bar{h}_{i,j}^{-3}}{\bar{r}_{i,j}} \left. \frac{\partial \bar{\theta}}{\partial \bar{\Psi}} \right|_{i,j}^t + \bar{\theta}_{i,j} \bar{h}_{i,j} \bar{r}_{i,j} \right) \quad (D30)$$

$$i = 1, \dots, m \quad j = 1, \dots, n$$

Additionally, the homogenized density ratio $\bar{\theta}^*$ and shear stresses $\bar{T}_{\bar{R},\bar{\Psi}}$ at the micro-scale are also defined by application of the trapezoid rule as (D31) and (D32),

$$\bar{\theta}^* = \frac{\Delta_{\bar{r}} \Delta_{\bar{\Psi}}}{8l_{\bar{r}} l_{\bar{\Psi}} \bar{R}} \sum_{i=1}^{i=m-1} \sum_{j=1}^{j=n-1} (\bar{r}_{i,j} + \bar{r}_{i+1,j}) (\bar{\theta}_{i,j} + \bar{\theta}_{i+1,j} + \bar{\theta}_{i,j+1} + \bar{\theta}_{i+1,j+1}) \quad (D31)$$

$$\begin{aligned} \bar{T}_{\bar{R},\bar{\Psi}_{1,2}} = \frac{\Delta_{\bar{r}} \Delta_{\bar{\Psi}}}{8l_{\bar{r}} l_{\bar{\Psi}} \bar{R}} \sum_{i=1}^{i=m-1} \sum_{j=1}^{j=n-1} (\bar{r}_{i,j} + \bar{r}_{i+1,j}) & \left(\bar{\tau}_{\bar{r},\bar{\Psi}_{1,2,i,j}} + \bar{\tau}_{\bar{r},\bar{\Psi}_{1,2,i+1,j}} + \bar{\tau}_{\bar{r},\bar{\Psi}_{1,2,i,j+1}} \right. \\ & \left. + \bar{\tau}_{\bar{r},\bar{\Psi}_{1,2,i+1,j+1}} \right) \end{aligned} \quad (D32)$$

where the discrete form of the micro-scale shear stresses are given by (D33) and (D34).

$$\bar{\tau}_{\bar{r}_{1,2,i,j}} = \pm \bar{g}_{i,j}^t \bar{h}_{i,j} \left. \frac{\partial \bar{\theta}}{\partial \bar{r}} \right|_{i,j}^t \quad (D33)$$

$$i = 1, \dots, m \quad j = 1, \dots, n$$

$$\bar{\tau}_{\bar{\Psi}_{1,2,i,j}} = \pm \frac{\bar{g}_{i,j}^t \bar{h}_{i,j}}{\bar{r}_{i,j}} \left. \frac{\partial \bar{\theta}}{\partial \bar{\Psi}} \right|_{i,j}^t + \frac{1}{3} \frac{\bar{r}_{i,j}}{\bar{h}_{i,j}} \quad (D34)$$

$$i = 1, \dots, m \quad j = 1, \dots, n$$